A detailed picture of Haiti's seismicity given by deep learning and template matching

Miguel Neves[1], Quentin Bletery[1], Françoise Courboulex[1], David Ambrois[1], Jérôme Chèze[1], Tony Monfret[1,2], Steeve Symithe[3], Sylvert Paul[1,3], Louis De Barros[1], Bryan Raimbault[4,5], and Éric Calais[4]

1. Observatoire de la Côte d'Azur, Université Côte d'Azur, IRD, CNRS, Geoazur, France.
2. Barcelona Center for Subsurface Imaging, Institut de Ciències del Mar (ICM), CSIC, Barcelona, Spain.
3. URGéo, Faculté des Sciences, Université d'État d'Haïti, Port-au-Prince, Haïti.
4. Département de Géosciences, École normale supérieure, Université PSL, Paris, France.
5. Univ. Grenoble Alpes, Univ. Savoie Mont Blanc, CNRS, IRD, Univ. Gustave Eiffel, ISTerre, Grenoble, France.

A detailed picture of Haiti's seismicity given by deep learning and template matching

Miguel Neves*,†1, Quentin Bletery[1], Françoise Courboulex[1], David Ambrois[1], Jérôme Chèze[1],
Tony Monfret[1,2], Steeve Symithe[3], Sylvert Paul[1,3], Louis De Barros[1], Bryan Raimbault[4,5], and Éric Calais[4]

ABSTRACT

Haiti regularly experiences destructive earthquakes, but seismic monitoring in the region has historically been limited. Recent deployments of citizen-hosted RaspberryShake seismometers and temporary seismic deployment following the 2021 $\mathrm{M_w}$ 7.2 earthquake provide new data to study the region's seismotectonics. However, high noise levels at many stations, in particular the RaspberryShake ones, limit detection, hence the fault imaging capability of these instruments. This study explores the use of a Deep Learning denoising algorithm, DeepDenoiser, to improve their seismic signal and earthquake detection capabilities. We find that DeepDenoiser raises the average signal-to-noise ratio of seismic signals by 4.7 dB and increases earthquake detections, but also raises false detections when using STA/LTA and a Deep Learning detection method. Template matching, however, when combined with DeepDenoiser, yields more true detections and fewer false detections than traditional band-pass filtered waveforms. This suggests that DeepDenoiser is better suited for retrospective studies than for real-time applications. Using DeepDenoiser and template matching, we compile a 2-year, high-resolution earthquake catalog for Haiti containing about 3 times the number of events of the original catalog. The improved catalog furthers our understanding of the 2021 $\mathrm{M_w}$ 7.2 earthquake sequence, highlighting particularly clearly the segmented nature of the aftershock distribution with a generally NE–dipping cluster in the east that coincides with the hypocenter and first reverse phase of the rupture, and a series of aftershocks farther west that coincide with the mostly strike-slip phase of the rupture. The improved catalog also reveals fluid-induced offshore seismic swarms in the Jérémie basin and active seismicity below Lake Enriquillo in the Dominican Republic. This catalog advances our knowledge of the region seismic activity and provides further opportunities to study the larger regional tectonic context.

INTRODUCTION

Our understanding of fault systems and earthquakes relies on regional efforts to monitor seismic activity and build comprehensive earthquake catalogs. Creating these catalogs involves multiple step workflows, including seismic data recording, earthquake detection, phase picking, association, location, and magnitude estimation. Historically, these efforts have relied on manual phase picking of seismic waveforms, but this becomes impractical with increasing data volumes. Energy-based automatic detection methods, such as the short-term-average to long-term-average (STA/LTA) trigger (Allen, 1978), have since been developed but provide coarser results, often generating false detections due to noise from non-tectonic impulsive signals, requiring manual review. As a result, earthquake catalogs are known to be incomplete (Kagan, 2004; Peng et al., 2006), particularly during time intervals of high background noise such as after a large earthquake.

Deep learning tools have emerged as a promising approach to monitor earthquake activity (Mousavi and Beroza, 2022) and address noise levels that hinder detection (Zhu et al., 2019). Algorithms like ConvNet (Ross et al., 2018), PhaseNet (Zhu and Beroza, 2019), or EQTransformer (Mousavi et al., 2020), can perform the critical step of phase picking – which is still routinely performed manually in most operational centers – with greater accuracy than traditional automatic algorithms (Allen, 1982). Recently proposed end-to-end algorithms can provide fast earthquake location and magnitude estimates directly from the waveforms (van den Ende and Ampuero, 2020; Münchmeyer et al., 2021; Lara et al., 2023, 2025; Licciardi et al., 2022; Hourcade et al., 2025), but still with lower accuracy than traditional methods (Kennett and Engdahl, 1991).

To improve earthquake catalog accuracy and completeness, several studies have developed denoising techniques that remove overlapping noise, improving the signal-to-noise ratio (SNR) of recorded seismic signals (e.g. Zhu et al., 2019; Mousavi and Langston, 2016, 2017). Unlike conventional spectral filtering, machine-learning denoisers adaptively separate target signals from noise, even in overlapping frequency bands (Zhu et al., 2019). While these techniques have the potential to improve SNR and detection rates, few studies have quantitatively evaluated their performance on continuously recorded waveforms (Yang et al., 2022; Dahmen et al., 2022).

In this study, we explore the potential gain in using recently developed deep learning tools for earthquake monitoring in Haiti. The island of Hispaniola, including Haiti and the Dominican Republic, is situated along a transpressional section of the Caribbean–north America plate boundary (Calais et al., 2016). This seismotectonic environment has resulted in numerous severe earthquakes throughout history (e.g. Bakun et al., 2012). More recently, the 2010 M_W 7.0 Haiti earthquake, one of the

---

1. Observatoire de la Côte d'Azur, Université Côte d'Azur, IRD, CNRS, Geoazur, France, https:// orcid.org/0000-0002-8581-8551 (MN) https://orcid.org/0000-0002-9796-5487 (QB) https:// orcid.org/0000-0002-4467-9102 (FC) https:// orcid.org/0000-0003-1155-5645 (DA) https:// orcid.org/0000-0002-7644-3989 (JC) https:// orcid.org/0000-0002-4521-0357 (TM) https:// orcid.org/0000-0003-4132-7635 (SP) https:// orcid.org/0000-0002-5541-9162 (LDB); 2. Barcelona Center for Subsurface Imaging, Institut de Ciències del Mar (ICM), CSIC, Barcelona, Spain, https://orcid.org/0000-0002-4521-0357 (TM); 3. URGéo, Faculté des Sciences, Université d'État d'Haïti, Port-au-Prince, Haïti, https://orcid.org/0000-0003-1133-202X (SS) https://orcid.org/0000-0003-4132-7635 (SP); 4. Département de Géosciences, École normale supérieure, Université PSL, Paris, France, https://orcid.org/0000-0001-9561-6171 (BR) https://orcid.org/0000-0002-5935-8117 (EC); 5. Univ. Grenoble Alpes, Univ. Savoie Mont Blanc, CNRS, IRD, Univ. Gustave Eiffel, ISTerre, Grenoble, France, https://orcid.org/0000-0001-9561-6171 (BR)

*Corresponding author: migueljgneves@gmail.com; †Now at Department of Earth Science, University of Bergen, Bergen, Norway

most consequential events in history, caused over 200,000 fatalities and economic losses close to 100% of the country's gross domestic product (Calais et al., 2010). Despite considerable natural, economical, and political obstacles (Corbet et al., 2024), Haiti has maintained an operational earthquake monitoring system (Calais et al., 2020, 2022). This system relies on citizen-hosted low-cost RS4D RaspberryShake (RS) seismic sensors (Figure 1) forming the network with code name HY (`https://doi.org/10.7914/sn/hy`). The data is streamed in real-time to a monitoring platform, coined Ayiti-seismes, which has operated continuously since August 2019. The platform uses data from the HY network, publicly open data streams from all temporary and permanent stations in the region (Paul et al., 2023) and an STA/LTA automatic detection method, followed by manual verification, to monitor seismicity in the region. The Ayiti-seismes system has enabled a significantly improved monitoring of the region with an estimated magnitude of completeness (M_C) of 2.5. The improved monitoring provided critical data to understand the 2021 M_W 7.2 Nippes earthquake (Calais et al., 2022), revealing a multiple segment rupture. This earthquake affected a mostly rural area, resulting in lower impacts than the 2010 earthquake – about 2,500 dead and 13,000 injured (OCHA, 2021) – but stressed the necessity of improving the Haiti earthquake catalog and our understanding of regional seismicity.

As reported by Paul et al. (2023), RS stations have higher noise levels than broadband stations on the island, because they are mostly located in urban environments, inside the homes of the citizens who volunteer to host them, and without prior in–depth verification of the background noise levels. Here, we test a deep learning tool to reduce noise levels in Haiti's seismic recordings. Combining the insights from our tests with the wealth of data from the HY network and a temporary seismic network composed of 12 broadband stations deployed in response to the 2021 M_W 7.2 Nippes earthquake (Z2, Douilly et al., 2022), we compile a high-resolution 2-year catalog (January 2021 to December 2022) that reveals previously unidentified clusters of seismic activity.

DENOISING

To enhance the quality of seismic waveforms recorded in Haiti, we apply the DeepDenoiser deep learning algorithm (Zhu et al., 2019). DeepDenoiser is a convolutional neural network trained to separate earthquake signals from noise in the frequency domain. It takes spectrograms of noisy signals as input and outputs a signal and a noise mask, which are applied to the input signal to obtain the denoised signal. The original DeepDenoiser model was trained on an extensive dataset of earthquake and noise signals recorded in northern California (Zhu et al., 2019).

We test different DeepDenoiser models before applying them to continuous Haiti data: 1) the original DeepDenoiser model (Zhu et al., 2019), 2) UrbanDenoiser – a version retrained on the Long Beach (California, USA) focusing on urban environments – (Yang et al., 2022), and 3) models retrained on Haiti data. For retraining, we use 4,957 30-second-long earthquake waveforms with SNR above 10 dB from the Ayiti-seismes catalog, and 5,976 noise waveforms listed as "Not earthquakes" after applying the PhaseNet picker (Zhu and Beroza, 2019) to ensure no seismic phase is present. The dataset is split into training, validation and testing datasets in a 80%/10%/10% ratio. We retrain the model starting with the original DeepDenoiser weights, testing different retraining approaches (entire network, first layer, last layer), learning rates (10^{-2} to 10^{-6}), batch sizes (50, 100, 200, 500), and dropout rates (0, 0.01, 0.05, 0.1, 0.25). We used cross-entropy loss and stopped training once there was no validation loss improvement for 10 epochs, saving the epoch with best validation loss. For each epoch, each signal waveform is merged with all noise waveforms randomly scaling its amplitude to create multiple "noisy" signals (Zhu et al., 2019). To assess performance, we calculate the SNR and signal distortion ratio (SDR) of the test dataset waveforms (Zhu et al., 2019; Yang et al., 2022) using:

$$SNR = 10\log_{10}\frac{\sigma_{signal}}{\sigma_{noise}}, \tag{1}$$

and

$$SDR = 10\log_{10}\frac{||W_{GT}||}{||W - W_{GT}||}, \tag{2}$$

where W is the denoised waveform, W_{GT} the ground truth waveform, σ_{signal} the standard deviation of the signal, and σ_{noise} the standard deviation of the noise. High SDR indicates lower distortion, reflecting better separation of the signal of interest from noise.

Results from our tests of transfer learning and fine-tuning DeepDenoiser models on the Haiti test dataset are shown in Table 1. We present only the best results for each combination of dropout rates, batch sizes, and learning rates. Based on SNR metrics, retraining the entire network or just the last layer shows a slight improvement over the original DeepDenoiser model. However, when considering the average SDR estimates, the retrained models perform worse than the original model. This suggests that retrained models remove more noise before the first phase arrival but also misidentify more signal as noise, leading to higher waveform distortion. Notably, the UrbanDenoiser model, trained on urban data with large anthropogenic noise, performs worse than the original DeepDenoiser model and any of the retrained models.

Based on these results, we choose to use the original DeepDenoiser model for denoising in the rest of this study (Figure 2) as it presents the best balance of SNR and SDR (Table 1).

We apply the original DeepDenoiser model to all P-phase picks in the Ayiti-seismes catalog, including those with SNR < 10 dB, and compute SNRs for denoised and non-denoised waveforms (Figure 3). The average SNR increases by 4.7 dB across the full dataset and by 4.3 dB for the RS stations, indicating that DeepDenoiser improves signal quality similarly for the entire catalog and for the RS instruments, even though waveforms from RS instruments were absent from the training set.

DETECTION

To assess the impact of denoising on earthquake detection, we apply three detection methods: the STA/LTA (Allen, 1978), PhaseNet deep learning picker (Zhu and Beroza, 2019), and template matching detection (Gibbons and Ringdal, 2006).

We perform detection on all the stations available in the island (Figure 1 and Table S1). To ensure a fair comparison, we established consistent source-station distances and corresponding detection time windows for analysis. We determined a distance threshold by examining the distribution of source-station distances for the earthquakes in our catalog (Figure S1a). This distribution exhibited a clear bimodal pattern, with a noticeable decrease in number of phase picks around 120 km, and a dominant first mode containing a higher number of phase picks. This bimodal shape reflects the island's geography, as most stations are concentrated in its western side. Therefore, we selected 120 km as the distance threshold, focusing our analysis on the dominant mode and local distances, similar to those used to train the DeepDenoiser and PhaseNet models (Zhu and Beroza, 2019; Zhu et al., 2019). This distance threshold corresponds to an approximate S-P time difference of 15 s (Figure S1b).

We apply STA/LTA and PhaseNet to single-station waveforms separately, whereas we apply template matching to the entire network waveforms. Therefore, we must perform association of the STA/LTA and PhaseNet phase picks, which we do using the Rapid Earthquake Association and Location method (REAL) (Zhang et al., 2019).

To compare the different detection methods, we apply them to band-pass filtered, denoised and denoised-and-band-pass-filtered waveforms. We then compare the number of detections and their quality by visual inspection. For PhaseNet, we also compare raw waveform detections. We apply DeepDenoiser to continuous data, using the Seisbench package tools (Woollam et al., 2022), processing 30 s windows of data with an overlap of 15 seconds (taking the average of overlapping segments).

STA/LTA

The STA/LTA method (Allen, 1982) is a detection technique widely used in real-time monitoring systems (e.g. Helmholtz-Centre Potsdam - GFZ German Research Centre for Geosciences and gempa GmbH, 2008). It computes the ratio of a short-term window's average (STA) amplitude to a long-term window's average (LTA) amplitude. Once this STA/LTA ratio exceeds a predefined threshold, a detection is declared. We test STA/LTA using the parameters used in Ayiti-seismes (Paul et al., 2023). We use ObsPy's recursive STA/LTA function (Beyreuther et al., 2010) with a 1 s short window, a 30 s long window and a trigger threshold of 2.5. Detection of P-phases is performed on the vertical components, and S-phases on the average envelope of the horizontal components.

PhaseNet

PhaseNet is a deep learning model that identifies seismic phase arrivals (Zhu and Beroza, 2019). PhaseNet is widely used in deep learning earthquake detection workflows (e.g. Liu et al., 2020; Tan et al., 2021; Wickham-Piotrowski et al., 2024). It analyzes three-component waveforms, evaluating the probability that a trace contains a P or S wave or noise. Similarly to the original DeepDenoiser model, the original PhaseNet was trained on waveforms from the northern California earthquake catalog. We use the Seisbench implemented PhaseNet model (Woollam et al., 2022), applying it to 30 s windows of 100 Hz continuous data with 15 s steps. A P- or S-phase detection is declared if the respective probability exceeds 0.1.

Association

In the case of STA/LTA and PhaseNet, we associate detected picks using REAL (Zhang et al., 2019). REAL is an associator that counts phase picks along theoretical travel-time windows, for which we use the velocity model inverted by Douilly et al. (2022). The grid search parameters we use for the theoretical travel time calculations are 1.2° with 0.05° steps for the horizontal distance and 40 km with 2 km steps for depth. We allow an earthquake detection every 10 seconds, limiting the maximum source-station distance to 120 km and requiring at least 4 P-phase picks and 2 S-phase picks for a detection.

Template Matching

Template matching detects similar seismic events by cross-correlating waveforms of cataloged events with continuous waveforms (e.g. Gibbons and Ringdal, 2006; Neves et al., 2022). We use events from Ayiti-seismes' catalog as templates, selecting events with at least 4 P-phase picks with source-station distances $<$ 120 km and SNR $>$ 5. For these events, we use a time window from 1 s before the P-phase arrival to 16 s after, including also the S-phase arrival. We cross-correlate the templates with continuous waveforms of the corresponding station using 1 hour segments with 1-sample steps. To improve the SNR of the cross-correlation function (CCF), we shift and stack the CCFs of the entire network and declare a detection if the stacked CCF is above 26 times the median absolute deviation.

Impact of denoising on earthquake detection

To assess the impact of denoising the waveforms recorded in Haiti considering the aforementioned detection methods, we visually inspect the obtained catalogs during two time intervals: from August 1 to August 26, an interval that includes detections prior to the deployment of the temporary broadband network and the early aftershock period of the 2021 mainshock, and November 6 and 7, the 2 days with the highest number of working stations in the dataset. Histograms summarizing the classification of detected events as real and false detections are shown in Figure 4. The detection methods were tested on band-passed filtered and denoised waveforms for all methods, and also on "raw" waveforms – *i.e,* removing only the trend – for PhaseNet detections, since PhaseNet was trained on unfiltered waveforms.

Considering only the detection numbers, PhaseNet applied to denoised waveforms returns the highest number of detections. However, when inspecting these detections, we find that more than 60% of them correspond to the detection and association of impulsive artifacts resulting from the denoising process. A similar result is obtained using STA/LTA with denoised waveforms: a higher number of events is detected but the majority corresponds to artifacts. For PhaseNet, the best ratio of real detections is observed when applying the detector with raw waveforms, even though it misses detections found only in denoised waveforms. In contrast, template matching performs best using denoised waveforms followed by a bandpass filter. This strategy returns fewer false detections and more real detections than applying template matching on only bandpass filtered waveforms or only denoised waveforms. It further returns a higher number of real detections than any strategy using PhaseNet and STA/LTA, and almost 1.5 times more real detections than template matching with bandpass filtered waveforms.

COMBINING DENOISING AND TEMPLATE MATCHING TO COMPILE A NEW CATALOG

Considering the performances of the methods tested here (Figure 4), we apply template matching detection to denoised and bandpass filtered (2–16 Hz) waveforms in order to build an enhanced earthquake catalog in Haiti. To do so, we use 2,065 templates and search in all continuous waveforms available from January 2021 to December 2022. Magnitudes of the newly detected events were estimated using relative magnitude estimation (see Supplemental File, Figure S3). The detection yields a catalog of 13,877 events, four times the 3,471 events in the Ayiti-seismes catalog considering the same 120 km source-station distance limit. We miss 1,824 Ayiti-seismes events due to our four recording stations within a 120 km radius requirement (Figure S4).

We locate the new events using HypoDD (Waldhauser and Ellsworth, 2000), which determines relative earthquake locations by minimizing observed and theoretical travel-time difference residuals for pairs of earthquakes recorded at the same station, reducing errors from velocity-model mismatches. We use cross-correlation-derived differential travel-times, computing the travel-time differences using denoised waveforms bandpass filtered between 2 and 16 Hz. We cross-correlate each event with all events in a 5 km radius or the 10 closest events – whichever is larger – using -0.2 to 1.3 s windows around P- and S-phase arrivals. We consider all measurements with a cross-correlation coefficient (CCC) > 0.6, and only keep pairs with at least 5 measurements and an average CCC > 0.7, ensuring at least 3 stations in common. To avoid measurements from spurious high CCC values, we recalculate CCCs using a 2 s window waveform and discard any travel-time measurement whose maximum CCC differs by more than 1 sample. We use the Douilly et al. (2022) velocity model to locate the events. The relocation results in a final catalog of 11,752 events (Figures 5-7 and S5). The majority of non-relocated events corresponds to the largest magnitude events, a consequence of deteriorated CCC measurements between events with large-magnitude differences (Bachura and Fischer, 2019). Additionally, poor waveform quality following the 2021 mainshock, with fewer continuously working stations and increased data gaps at this time, results in a significant number of non-relocated events (325) in the 10 days after the mainshock.

To confirm the positive impact of denoising on the final catalog, we apply the same template matching detection and relocation procedure to only bandpass filtered waveforms (2–16 Hz) for August to November 2021. This test results in a catalog of 6,774 events using the filtered waveforms compared to 7,393 events when using denoised waveforms. Furthermore, using filtered waveforms, the relocated events pair on average with 59 events and have an average relative location uncertainty of

20 m, whereas using the denoised waveforms, each event pairs on average with 100 events and have an average uncertainty of 14 m. Template matching is the biggest net contributor to the improved catalog, but denoising further reveals new events and improves locations by providing more differential travel-time information data.

The final catalog presents 11,752 precisely located events, which is about 3 times the number of events in the Ayiti-seismes catalog for the same time interval (3,992). Most of the newly detected events are located in the 2021 Nippes mainshock area, but the new catalog also reveals clear clusters of seismicity in other regions like the Jérémie Basin and the Enriquillo lake in Dominican Republic. We note that our catalog is biased towards sources similar to those already present in the Ayiti-seismes catalog due to the characteristics of template matching and double-difference relocation, limiting improvements for background or isolated seismicity.

DISCUSSION

On the use of denoising for earthquake monitoring in Haiti

Our findings indicate that DeepDenoiser is better suited for detailed seismicity analyses than for automatic detection workflows. Our comparative tests using STA/LTA (Figure 4a), the method used by Ayiti-seismes and commonly adopted by earthquake monitoring agencies (e.g. Duverger et al., 2021; González, 2017), reveal that denoising significantly increases false alerts, increasing analysts' workload. Additionally, employing DeepDenoiser followed by a band-pass filter yields fewer detections compared to traditional band-pass filtering. This discrepancy arises from variations in picking times that complicate the association process. DeepDenoiser zeros the amplitude of segments deemed pure noise, leading to subtle fluctuations being misinterpreted as phase onsets. Consequently, P-phases are often picked earlier than manual picks or from the standard STA/LTA method. Combining DeepDenoiser with PhaseNet increases both false and real detections (Figure 4b). However, PhaseNet was not retrained on local nor denoised waveforms; it is therefore possible that better results can be achieved in any of these situations. Template matching shows a clear improvement applying DeepDenoiser and band-pass filtering (Figure 4c), yielding more real detections and fewer false ones. However, despite the existence of near-real-time template matching systems (Chamberlain et al., 2020), the method's computational cost and reliance on existing templates make it better suited for detailed retrospective analyses.

We therefore advise caution when deploying DeepDenoiser directly in automated earthquake monitoring. In its current form it is unsuitable for the Ayiti-seismes workflow, but improvements are possible: augment the training set with additional RS recordings which have different coupling and noise levels, incorporate intervals containing artifacts identified by both STA/LTA and PhaseNet into the noise samples, and explore physics-based denoising methods that enforce real-world constraints (Banerjee et al., 2024).

A detailed picture of the 2021 mainshock area

The majority of the events – about 67%, or 7,948 earthquakes – in our new high-resolution catalog lies in the area of the 2021 M_w 7.2 Nippes earthquake (Figs. 5 and 6). In this region we find 4.8 times more events than in the Ayiti-seismes system catalog (7,948 vs 1,662 on the same time interval) and 2.7 more events than in the catalog of Douilly et al. (2022) (6,422 vs 2,417 from 20 August 2021 to 30 December 2021). The additional detections and improved locations provide a more detailed picture of the 2021 sequence and the involved fault segments (Figure 8).

The 2021 M_w 7.2 Nippes earthquake ruptured near the Enriquillo-Plantain Garden Fault (EPGF) (Calais et al., 2020), an east-west left-lateral strike-slip fault that spans Haiti's southern Peninsula and extends offshore toward Jamaica (Mann et al., 1995). Inversions of seismic and geodetic data show that the mainshock rupture initiated on a mostly reverse-fault segment and propagated westward to a mostly strike-slip segment (Calais et al., 2022). Raimbault et al. (2023) identified two distinct segments: a first one dipping 66° N and mostly reverse, and a second one farther west dipping 86°north and mostly strike-slip, associated with the Ravine du Sud fault (RSF). Douilly et al. (2022) also identified a multiple-segment structure, with a western segment connected to the RSF and two eastern segments dipping 60°and 70° N. They noted a near-vertical aftershock cluster near the expected EGPF extent at depth, interpreted as triggered seismicity on the EPGF, which they suggested did not rupture coseismically. Paul et al. (2025) expanded the aftershock catalog of Douilly et al. (2022) and applied the NLL-SSST-Coherence location method (Lomax and Savvaidis, 2022), identifying two clusters: a narrow western cluster parallel to the EPGF, steeply dipping northward and interpreted as the EPGF at depth; and a broader ~N110–trending cluster dipping ~70°north, interpreted as a separate reverse fault, termed the "Nippes fault".

As in those two catalogs, the aftershock distribution found here also delineates two clusters with different orientations. We analyze the aftershock distribution by examining the dip variations of the seismic clusters shown in Figure 8. Events in the western part (segments AA', BB' and CC' in Figure 8) generally show a near-vertical distribution, albeit discontinuous, with a clearer lineament in segment CC'. Between 73.81° W and 73.63° W (segment DD', Figure 8e) the aftershock distribution becomes more complex showing events still associated with the CC' near-vertical lineament, and additional events north of it also showing near-vertical trends. Towards the center of segment DD', a north-dipping cluster appears below 10 km, with a small gap to the west. West of 73.63° W, a large and complex cluster coincides with the mainshock hypocenter and most aftershocks (segment EE'). We model this cluster by dividing it into several fault planes with equal longitudinal extent. Testing partitions from 1 to 10 planes, we select the configuration with the lowest sum of squared differences between the observed aftershock locations and the modeled planes. The cluster is best explained by 5 planes (shown in shades of green in Figure 8a and respective cross-sections in Figs. 8g-k). Consistent with (Douilly et al., 2022) and Paul et al. (2025), this structure strikes WSW-ENE in the west, gradually rotating to an almost NW-SE strike to the west, up until 73.48° W where it returns to an almost E-W strike. This structure retains a northward dip of 55°to 78°throughout its length.

The aftershock distribution aligns well with the rupture geometry and coseismic slip distribution inferred from geodetic data by Raimbault et al. (2023), shown with colored contours in Figure 8. The main cluster bends around the peak slip of their 66°north-dipping structure (Figure 8a), in-line with our aftershock distribution dip estimates. To the west, aftershocks in segments BB', CC', and DD' agree with the 86°north-dipping strike-slip segment of Raimbault et al. (2023), particularly in segment CC', which shows a similar near-vertical dip. The observed gap in segment DD' coincides with the meeting point of the strike-slip and reverse rupture segments found by Raimbault et al. (2023).

A significant difference between our catalog and that of Douilly et al. (2022) pertains to the distribution of aftershocks in segment EE' closer to the surface trace of the EGPF. This previous catalog shows a near-vertical cluster at 5-10 km depths close to the expected fault location. In our catalog, events at this location dip northward and align well with the previous modeled planes. This suggests these events are part of the reverse fault where the mainshock initiated. We find no evidence of aftershocks associated with a vertically-dipping EPGF in this area.

Fluid-induced seismic swarms in the Jérémie basin?

Our new catalog reveals several offshore earthquake clusters in the Jérémie basin, NW of the 2021 mainshock epicenter (Figure 9), also present in the Ayiti-séismes catalog (Figure 5) but with a more spread-out distribution. Here, we identify six clusters (C1 to C6) shown in Figure 9a. Cluster C1, the earliest and largest (2,136 events), and clusters C2 (216 events) and C3 (358 events) are located near shallow reverse faults in the Jérémie–Malpasse fault system (Calais et al., 2023). Clusters C1 and C3 delineate very low-angle SW-dipping structures consistent with identified thrust faults. Cluster C3 shows two SW-dipping lineaments at depths of 11 km and 15 km (Figures S7). Cluster C2 shows a similar shallow and deeper group but without clear lineaments (Figure S6). Cluster C4 (48 events) is a shallow group of events at less than 3 km depth that extends in the E-W direction and shows a SSE dipping (Figure S8). Clusters C5 (123 events) and C6 (38 events) do not define clear lineaments, with C5 located above 2 km depth and C6 concentrating around 11 km depth.

These clusters present swarm-like characteristics with no clear mainshock (Mogi, 1963). For example, the largest earthquake in cluster C1 is a M 4.8 event occurring 128 days after the onset. Cluster C1 also shows a clear NW migration pattern. Earthquake swarms are usually explained as resulting from fluid pressure diffusion (e.g. Shapiro et al., 1997), aseismic slip (e.g. Roland and McGuire, 2009), or an interplay of both (e.g. Hainzl, 2004; De Barros et al., 2020). We test this hypothesis by defining a propagation front adapting the methodology of previous studies (Amezawa et al., 2021; Danré et al., 2022). Considering the evolution of event distance to the initial event of each cluster, we define the front as the 90th percentile of the distance in non-overlapping bins of 25 events for clusters with more than 100 events, and 10 events for smaller clusters. We fit three models to the front (Danré et al., 2024; Adeboboye et al., 2025): fluid pressure diffusion described by $R = \sqrt{4\pi Dt}$, where R is the distance to the origin of the pressure source, D the diffusivity and t time (Shapiro et al., 1997); linear migration; and constant distance, to test the absence of migration. Clusters C1, C3, and C4 migration is best explained by the fluid diffusion model (Figures 9d, S7d,e, and S8d); although in the case of C4 it is not significantly different than the constant case. These results are consistent with the observed activity in the Jérémie basin being driven by fluids. Inferred diffusivities (0.14 m^2/s for C1, 0.004-0.04 m^2/s for the others) fall into the range observed in other fluid-driven swarms (Talwani et al., 2007). The estimated migration velocity and swarm duration, for example 38 m/day $\sim 4\times 10^{-4}$ m/s and 160 days $\sim 1.4\times 10^{7}$ s for cluster C1, also fall in the middle of the scaling law empirically derived by Danré et al. (2024) for fluid-induced swarms, comforting the hypothesis that the swarms are driven by fluid migration processes.

Evidence for seismic activity in Lake Enriquillo

The extension of the EPGF is well-documented in southern Haiti until about 72.27° W (Symithe and Calais, 2016). Further east, its extension is still debated. Mann et al. (1995) proposed that the EPGF continues eastward through the Enriquillo-Cul-de-Sac Valley into Lake Enriquillo, Dominican Republic, based on *en échelon* faults and folds (Figure 10). Lake Enriquillo is bounded by active thrust faults (Mann et al., 1995) where moderate seismic activity has been recorded (Escuder-Viruete et al., 2025; Rodriguez et al., 2018; Possee et al., 2019; Lee and Douilly, 2022). Mann et al. (1995) proposed that the EPGF extends continuously to the east along the northern edge of Cabritos Island in Lake Enriquillo on the basis of subvertical zone of incoherent reflections on a seismic profile, though reflectors at depth on this profile are continuous across and not affected by faulting. Wang et al. (2018) analyzed high-resolution sonar data and proposed a continuous extension of the EPGF until at least Cabritos Island with evidence for recent activity, though again the data do not document faulting at depth. In contrast with this proposal of a continuous extent of the EPGF throughout Cul-de-Sac – Enriquillo basin, Symithe and Calais (2016) posit that the EPGF stops around about 72.27° W and abuts against a series of reverse faults and fold–propagation folds that extends along the southern edge of the basin. This interpretation is shared by other authors on the basis of field observations (Saint Fleur et al., 2019; Wessels et al., 2019; Escuder-Viruete et al., 2025) and of earthquake distribution (Rodriguez et al., 2018; Possee et al., 2019) in southern Haiti and Dominican Republic.

Our new catalog does not resolve the eastern extent of the EPGF, but documents seismic activity near Cabritos Island (Figure 10). We identify 62 earthquakes along the island's northern edge, where Mann et al. (1995) proposed the EPGF continuation. The events occur mostly in two distinct bursts, with a group of 47 events from July 21 to August 5, 2021, the largest one of M 3.2, then a group of 14 events from July 16 to July 20, 2022, the largest one of M 2.0. The seismicity extends from 4 to 11 km depth but does not align on a single, throughgoing, vertical structure. Part of the larger cluster (orange on Figure 10a) appears near-vertical, but most of it actually follows a quasi-horizontal plane just above 5 km depth. The magnitudes of the recorded earthquakes and the limited azimuthal station coverage preclude us from determining focal mechanisms that would shed light on the fault kinematics associated with the observed seismicity.

CONCLUSIONS

We explored the applicability of a deep learning denoising tool, DeepDenoiser, for seismic monitoring in Haiti. We found it is more suitable for retrospective detailed seismicity studies than for real-time application. When combined with template matching, DeepDenoiser enhances detection rates while reducing false positives. Doing so, we enhanced the description of Haiti's earthquake activity tripling the number of events compared to existing catalogs. The catalog we obtained provides a detailed view of the 2021 M_w 7.2 Nippes earthquake, with aftershock distribution agreeing with recent coseismic slip models (Raimbault et al., 2023) and no evidence of aftershocks associated with a vertical EPGF. It also reveals offshore swarms in the Jérémie basin with fluid-driven migration patterns and a distinct group of events in Lake Enriquillo, Dominican Republic, coinciding with a proposed EPGF continuation. These results show that denoising can enhance catalog completeness and quality, revealing previously unidentified areas of active seismic activity in Hispaniola.

DATA AND RESOURCES

The detection and relocated catalogs are included as supplementary files (Supplemental Datasets S1 and S2). The Ayiti-seismes earthquake catalog and data from the HY network are available at the Ayiti-seismes platform (`https://ayiti.unice.fr/ayiti-seismes`). Data from networks AY, CN (Natural Resources Canada, 1975), CU (Albuquerque Seismological Laboratory (ASL)/USGS, 2006), DR (National Seismological Centre, 1998), LO (Instituto Politecnico Loyola, 2012) can be accessed through IRIS Web Services (`https://service.iris.edu/`). Z2 network data will be available through IRIS Web Services in October 2026.

DECLARATION OF COMPETING INTERESTS

The authors declare no conflicts of interest.

ACKNOWLEDGMENTS

We acknowledge funding from the FEDER program through the Interreg Caraïbes "PREST" project (grant 5236), the French National Research Agency "OSMOSE" (ANR-21CE03-0010) and "CAST" (ANR-22-CE01-0019) projects, and support from the Joint International Laboratory "Caribact". Steeve J. Symithe acknowledges support from Grant and Cooperative Agreement G20AC00100 between the U.S. Geological Survey and the Faculté des Sciences of the State University of Haiti, funded by the USAID Bureau of Humanitarian Assistance, and support from the Fonds d'Appui à la Recherche of the Rectorat of the State University of Haiti. We thank Roby Douilly for providing access to the Z2 network.

REFERENCES

Adeboboye, O. E., L. Y. Chuang, M. Neves, Z. Peng, D. Frost, and S. C. Jaumé (2025). Localized west-dipping seismic structure defines the elgin–lugoff swarm sequence in south carolina. *Seismological Research Letters* **96**(3), 2011–2026.

Albuquerque Seismological Laboratory (ASL)/USGS (2006). Caribbean network.

Allen, R. (1982). Automatic phase pickers: Their present use and future prospects. *Bulletin of the Seismological Society of America* **72**, S225–S242.

Allen, R. V. (1978). Automatic earthquake recognition and timing from single traces. *Bulletin of the seismological society of America* **68**(5), 1521–1532.

Amezawa, Y., T. Maeda, and M. Kosuga (2021). Migration diffusivity as a controlling factor in the duration of earthquake swarms. *Earth, Planets and Space* **73**(1).

Bachura, M. and T. Fischer (2019, 08). Waveform cross-correlation for differential time measurement: Bias and limitations. *Seismological Research Letters* **90**(5), 2005–2014.

Bakun, W. H., C. H. Flores, and U. S. ten Brink (2012). Significant Earthquakes on the Enriquillo Fault System, Hispaniola, 1500–2010: Implications for Seismic Hazard. *Bulletin of the Seismological Society of America* **102**(1), 18–30.

Banerjee, C., K. Nguyen, C. Fookes, and K. George (2024). Physics-Informed Computer Vision: A Review and Perspectives. *ACM Comput. Surv.* **57**(1), 17:1–17:38.

Beyreuther, M., R. Barsch, L. Krischer, T. Megies, Y. Behr, and J. Wassermann (2010). Obspy: A python toolbox for seismology. *Seismological Research Letters* **81**(3), 530–533.

Calais, E., D. Boisson, S. Symithe, C. Prépetit, B. Pierre, S. Ulyse, L. Hurbon, A. Gilles, J.-M. Théodat, T. Monfret, et al. (2020). A socio-seismology experiment in haiti. *Frontiers in Earth Science* **8**, 542654.

Calais, E., A. Freed, G. Mattioli, F. Amelung, S. Jónsson, P. Jansma, S.-H. Hong, T. Dixon, C. Prépetit, and R. Momplaisir (2010). Transpressional rupture of an unmapped fault during the 2010 haiti earthquake. *Nature Geoscience* **3**(11), 794–799.

Calais, E., S. Symithe, B. M. de Lepinay, and C. Prepetit (2016). Plate boundary segmentation in the northeastern caribbean from geodetic measurements and neogene geological observations. *Comptes Rendus. Géoscience* **348**(1), 42–51.

Calais, E., S. Symithe, T. Monfret, B. Delouis, A. Lomax, F. Courboulex, J. P. Ampuero, P. E. Lara, Q. Bletery, J. Chèze, et al. (2022). Citizen seismology helps decipher the 2021 haiti earthquake. *Science* **376**(6590), 283–287.

Calais, E., S. J. Symithe, and B. M. de Lépinay (2023). Strain partitioning within the caribbean–north america transform plate boundary in southern haiti, tectonic and hazard implications. *Bulletin of the Seismological Society of America* **113**(1), 131–142.

Chamberlain, C. J., J. Townend, and M. C. Gerstenberger (2020). RT-EQcorrscan: Near-Real-Time Matched-Filtering for Rapid Development of Dense Earthquake Catalogs. *Seismological Research Letters* **91**(6), 3574–3584.

Corbet, A., J. Célestin, L. Fallou, N. Calixte, S. Steeve, and E. Calais (2024). Qu'est-ce que faire de la science citoyenne dans un pays sans citoyens"? *Etudes caribeennes* **59**.

Dahmen, N. L., J. F. Clinton, M.-A. Meier, S. C. Stähler, S. Ceylan, D. Kim, A. E. Stott, and D. Giardini (2022). MarsQuakeNet: A More Complete Marsquake Catalog Obtained by Deep Learning Techniques. *Journal of Geophysical Research: Planets* **127**(11), e2022JE007503. e2022JE007503 2022JE007503.

Danré, P., L. De Barros, F. Cappa, and J.-P. Ampuero (2022). Prevalence of aseismic slip linking fluid injection to natural and anthropogenic seismic swarms. *Journal of Geophysical Research: Solid Earth* **127**(12), e2022JB025571. e2022JB025571 2022JB025571.

Danré, P., L. De Barros, F. Cappa, and L. Passarelli (2024). Parallel dynamics of slow slips and fluid-induced seismic swarms. *Nature Communications* **15**(1), 8943.

De Barros, L., F. Cappa, A. Deschamps, and P. Dublanchet (2020). Imbricated Aseismic Slip and Fluid Diffusion Drive a Seismic Swarm in the Corinth Gulf, Greece. *Geophysical Research Letters* **47**(9), e2020GL087142.

Douilly, R., S. Paul, T. Monfret, A. Deschamps, D. Ambrois, S. J. Symithe, S. St Fleur, F. Courboulex, E. Calais, D. Boisson, B. M. de Lépinay, Y. Font, and J. Chèze (2022). Rupture Segmentation of the 14 August 2021 Mw 7.2 Nippes, Haiti, Earthquake Using Aftershock Relocation from a Local Seismic Deployment. *Bulletin of the Seismological Society of America* **113**(1), 58–72.

Duverger, C., G. Mazet-Roux, L. Bollinger, A. Guilhem Trilla, A. Vallage, B. Hernandez, and Y. Cansi (2021). A decade of seismicity in metropolitan France (2010–2019): the CEA/LDG methodologies and observations. *Bulletin de la Société Géologique de France* **192**(1), 25.

Escuder-Viruete, J., F. J. Fernández, F. P. Valera, A. Medialdea, and M. Castillo-Carrión (2025). Present-day shortening accommodated by folding, thrusting and strike-slip faulting in the enriquillo basin of southern central hispaniola: Implications for the regional seismic hazard. *Tectonics* **44**(1), e2024TC008376. e2024TC008376 2024TC008376.

Gibbons, S. J. and F. Ringdal (2006). The detection of low magnitude seismic events using array-based waveform correlation. *Geophysical Journal International* **165**, 149–166.

González, A. (2017). The Spanish National Earthquake Catalogue: Evolution, precision and completeness. *Journal of Seismology* **21**(3), 435–471.

Hainzl, S. (2004). Seismicity patterns of earthquake swarms due to fluid intrusion and stress triggering. *Geophysical Journal International* **159**(3), 1090–1096.

Helmholtz-Centre Potsdam - GFZ German Research Centre for Geosciences and gempa GmbH (2008). The SeisComP seismological software package. GFZ Data Services.

Hourcade, C., K. Juhel, and Q. Bletery (2025). Pegsgraph: A graph neural network for fast earthquake characterization based on prompt elastogravity signals. *Journal of Geophysical Research: Machine Learning and Computation* **2**(1), e2024JH000360.

Instituto Politecnico Loyola (2012). Observatorio sismológico politécnico loyola.

Kagan, Y. Y. (2004). Short-term properties of earthquake catalogs and models of earthquake source. *Bulletin of the Seismological Society of America* **94**(4), 1207–1228.

Kennett, B. and E. Engdahl (1991). Traveltimes for global earthquake location and phase identification. *Geophysical Journal International* **105**(2), 429–465.

Lara, P., Q. Bletery, J.-p. Ampuero, A. Inza, and H. Tavera (2023). Earthquake early warning starting from 3 s of records on a single station with machine learning. *Journal of Geophysical Research: Solid Earth* **128**(11), e2023JB026575.

Lara, P., H. Tavera, Q. Bletery, J.-P. Ampuero, A. Inza, D. Portugal, B. Orihuela, and F. Meza (2025). Implementation of the peruvian earthquake early warning system. *Bulletin of the Seismological Society of America* **115**(1), 191–209.

Lee, H. and R. Douilly (2022). Earthquake Swarms in Southern Hispaniola Revealed by Spatiotemporal Evolution of Seismicity from Multi-Station Template Matching. *Bulletin of the Seismological Society of America* **113**(1), 115–130.

Licciardi, A., Q. Bletery, B. Rouet-Leduc, J.-P. Ampuero, and K. Juhel (2022). Instantaneous tracking of earthquake growth with elastogravity signals. *Nature* **606**(7913), 319–324.

Liu, M., M. Zhang, W. Zhu, W. L. Ellsworth, and H. Li (2020). Rapid characterization of the july 2019 ridgecrest, california, earthquake sequence from raw seismic data using machine-learning phase picker. *Geophysical Research Letters* **47**(4), e2019GL086189.

Lomax, A. and A. Savvaidis (2022). High-precision earthquake location using source-specific station terms and inter-event waveform similarity. *Journal of Geophysical Research: Solid Earth* **127**(1), e2021JB023190. e2021JB023190 2021JB023190.

Mann, P., F. W. Taylor, R. L. Edwards, and T.-L. Ku (1995). Actively evolving microplate formation by oblique collision and sideways motion along strike-slip faults: An example from the northeastern Caribbean plate margin. *Tectonophysics* **246**(1), 1–69.

Mogi, K. (1963). Some discussions on aftershocks, foreshocks and earthquake swarms-the fracture of a semi finite body caused by an inner stress origin and its relation to the earthquake phenomena. *Bull. Earthq. Res. Inst.* **41**, 615–658.

Mousavi, S. M. and G. C. Beroza (2022). Deep-learning seismology. *Science* **377**(6607), eabm4470.

Mousavi, S. M., W. L. Ellsworth, W. Zhu, L. Y. Chuang, and G. C. Beroza (2020). Earthquake transformer—an attentive deep-learning model for simultaneous earthquake detection and phase picking. *Nature communications* **11**(1), 3952.

Mousavi, S. M. and C. A. Langston (2016). Hybrid Seismic Denoising Using Higher-Order Statistics and Improved Wavelet Block Thresholding. *Bulletin of the Seismological Society of America* **106**(4), 1380–1393.

Mousavi, S. M. and C. A. Langston (2017). Automatic noise-removal/signal-removal based on general cross-validation thresholding in synchrosqueezed domain and its application on earthquake data. *Geophysics* **82**(4), V211–V227.

Münchmeyer, J., D. Bindi, U. Leser, and F. Tilmann (2021). Earthquake magnitude and location estimation from real time seismic waveforms with a transformer network. *Geophysical Journal International* **226**(2), 1086–1104.

National Seismological Centre (1998). Centro nacional de sismologia.

Natural Resources Canada (1975). Canadian national seismograph network.

Neves, M., Z. Peng, and G. Lin (2022, 11). A high-resolution earthquake catalog for the 2004 mw 6 parkfield earthquake sequence using a matched filter technique. *Seismological Research Letters* **94**(1), 507–521.

Paul, S., T. Monfret, E. Calais, F. Courboulex, D. Bertrand, A. Lomax, B. de Lépinay, S. Symithe, D. Anne, D. Ambrois, S. St Fleur, and D. Boisson (2025). Precise Relocation of the 14 August 2021 Mw 7.2 Nippes, Haiti, Earthquake Sequence using Broadband and Citizen-hosted Short-period Seismometers. *https://ssrn.com/abstract=5437094*.

Paul, S., T. Monfret, F. Courboulex, J. Chèze, E. Calais, S. Julien Symithe, A. Deschamps, F. Peix, D. Ambrois, X. Martin, S. St Fleur, and D. Boisson (2023, 09). Monitoring of local earthquakes in haiti using low-cost, citizen-hosted seismometers and regional broadband stations. *Seismological Research Letters* **94**(6), 2725–2739.

Peng, Z., J. E. Vidale, and H. Houston (2006). Anomalous early aftershock decay rate of the 2004 mw6. 0 parkfield, california, earthquake. *Geophysical Research Letters* **33**(17).

Possee, D., D. Keir, N. Harmon, C. Rychert, F. Rolandone, S. Leroy, J. Corbeau, G. Stuart, E. Calais, F. Illsley-Kemp, D. Boisson, R. Momplaisir, and C. Prépetit (2019). The Tectonics and Active Faulting of Haiti from Seismicity and Tomography. *Tectonics* **38**(3), 1138–1155.

Raimbault, B., R. Jolivet, E. Calais, S. Symithe, Y. Fukushima, and P. Dubernet (2023). Rupture geometry and slip distribution of the mw 7.2 nippes earthquake, haiti, from space geodetic data. *Geochemistry, Geophysics, Geosystems* **24**(4), e2022GC010752.

Rodriguez, J., J. Havskov, M. B. Sørensen, and L. F. Santos (2018, July). Seismotectonics of south-west Dominican Republic using recent data. *Journal of Seismology* **22**(4), 883–896.

Roland, E. and J. J. McGuire (2009). Earthquake swarms on transform faults. *Geophysical Journal International* **178**(3), 1677–1690.

Ross, Z. E., M.-A. Meier, E. Hauksson, and T. H. Heaton (2018). Generalized seismic phase detection with deep learning. *Bulletin of the Seismological Society of America* **108**(5A), 2894–2901.

Saint Fleur, N., N. Feuillet, and Y. Klinger (2019, November). Active tectonics along the Cul-de-Sac – Enriquillo plain and seismic hazard for Port-au-Prince, Haiti. *Tectonophysics* **771**, 228235.

Shapiro, S. A., E. Huenges, and G. Borm (1997). Estimating the crust permeability from fluid-injection-induced seismic emission at the ktb site. *Geophysical Journal International* **131**(2), F15–F18.

Styron, R., J. García-Pelaez, and M. Pagani (2020). Ccaf-db: the caribbean and central american active fault database. *Natural Hazards and Earth System Sciences* **20**(3), 831–857.

Symithe, S. and E. Calais (2016). Present-day shortening in southern haiti from gps measurements and implications for seismic hazard. *Tectonophysics* **679**, 117–124.

Talwani, P., L. Chen, and K. Gahalaut (2007). Seismogenic permeability, ks. *Journal of Geophysical Research: Solid Earth* **112**(B7).

Tan, Y. J., F. Waldhauser, W. L. Ellsworth, M. Zhang, W. Zhu, M. Michele, L. Chiaraluce, G. C. Beroza, and M. Segou (2021). Machine-learning-based high-resolution earthquake catalog reveals how complex fault structures were activated during the 2016–2017 central italy sequence. *The Seismic Record* **1**(1), 11–19.

United Nations Office for the Coordination of Humanitarian Affairs (OCHA) (2021). Haïti : Tremblement de terre Rapport de Situation No. 2 Au 26 Août 2021.

van den Ende, M. P. and J.-P. Ampuero (2020). Automated seismic source characterization using deep graph neural networks. *Geophysical Research Letters* **47**(17), e2020GL088690.

Waldhauser, F. and W. L. Ellsworth (2000). A Double-Difference Earthquake Location Algorithm: Method and Application to the Northern Hayward Fault, California. *Bulletin of the Seismological Society of America* **90**(6), 1353–1368.

Wang, J., P. Mann, and R. R. Stewart (2018). Late holocene structural style and seismicity of highly transpressional faults in southern haiti. *Tectonics* **37**(10), 3834–3852.

Wessels, R. J., N. Ellouz-Zimmermann, N. Bellahsen, Y. Hamon, C. Rosenberg, R. Deschamps, R. Momplaisir, D. Boisson, and S. Leroy (2019, January). Polyphase tectonic history of the Southern Peninsula, Haiti: From folding-and-thrusting to transpressive strike-slip. *Tectonophysics* **751**, 125–149.

Wickham-Piotrowski, A., Y. Font, M. Regnier, B. Delouis, O. Lengliné, M. Segovia, and Q. Bletery (2024). Achieving a comprehensive microseismicity catalog through a deep-learning-based workflow: Applications in the central ecuadorian subduction zone. *Bulletin of the Seismological Society of America* **114**(2), 823–841.

Woessner, J. and S. Wiemer (2005). Assessing the quality of earthquake catalogues: Estimating the magnitude of completeness and its uncertainty. *Bulletin of the Seismological Society of America* **95**(2), 684–698.

Woollam, J., J. Münchmeyer, F. Tilmann, A. Rietbrock, D. Lange, T. Bornstein, T. Diehl, C. Giunchi, F. Haslinger, D. Jozinović, A. Michelini, J. Saul, and H. Soto (2022). SeisBench—A Toolbox for Machine Learning in Seismology. *Seismological Research Letters* **93**(3), 1695–1709.

Yang, L., X. Liu, W. Zhu, L. Zhao, and G. C. Beroza (2022). Toward improved urban earthquake monitoring through deep-learning-based noise suppression. *Science Advances* **8**(15), eabl3564.

Zhang, M., W. L. Ellsworth, and G. C. Beroza (2019). Rapid Earthquake Association and Location. *Seismological Research Letters* **90**(6), 2276–2284.

Zhu, W. and G. C. Beroza (2019). PhaseNet: A deep-neural-network-based seismic arrival-time picking method. *Geophysical Journal International* **216**(1), 261–273.

Zhu, W., S. M. Mousavi, and G. C. Beroza (2019). Seismic Signal Denoising and Decomposition Using Deep Neural Networks. *IEEE Transactions on Geoscience and Remote Sensing* **57**(11), 9476–9488.

Miguel Neves
Universitetet i Bergen
Institutt for geovitenskap
Postboks 7803
5020 Bergen
Norway
migueljgneves@gmail.com

TABLE 1

Signal-to-noise ratio (SNR) and signal distortion ratio (SDR) for the different pretrained and retrained DeepDenoiser models. We show only the best result of the different hyperparameters.

		Pretrained		Retrained DeepDenoiser		
	Raw waveforms	DeepDenoiser	UrbanDenoiser	Entire Network	Last Layer	First Layer
SNR	15	34.42	17.66	35.44	32.51	34.86
SDR	-	6.74	6.48	5.36	4.59	5.83

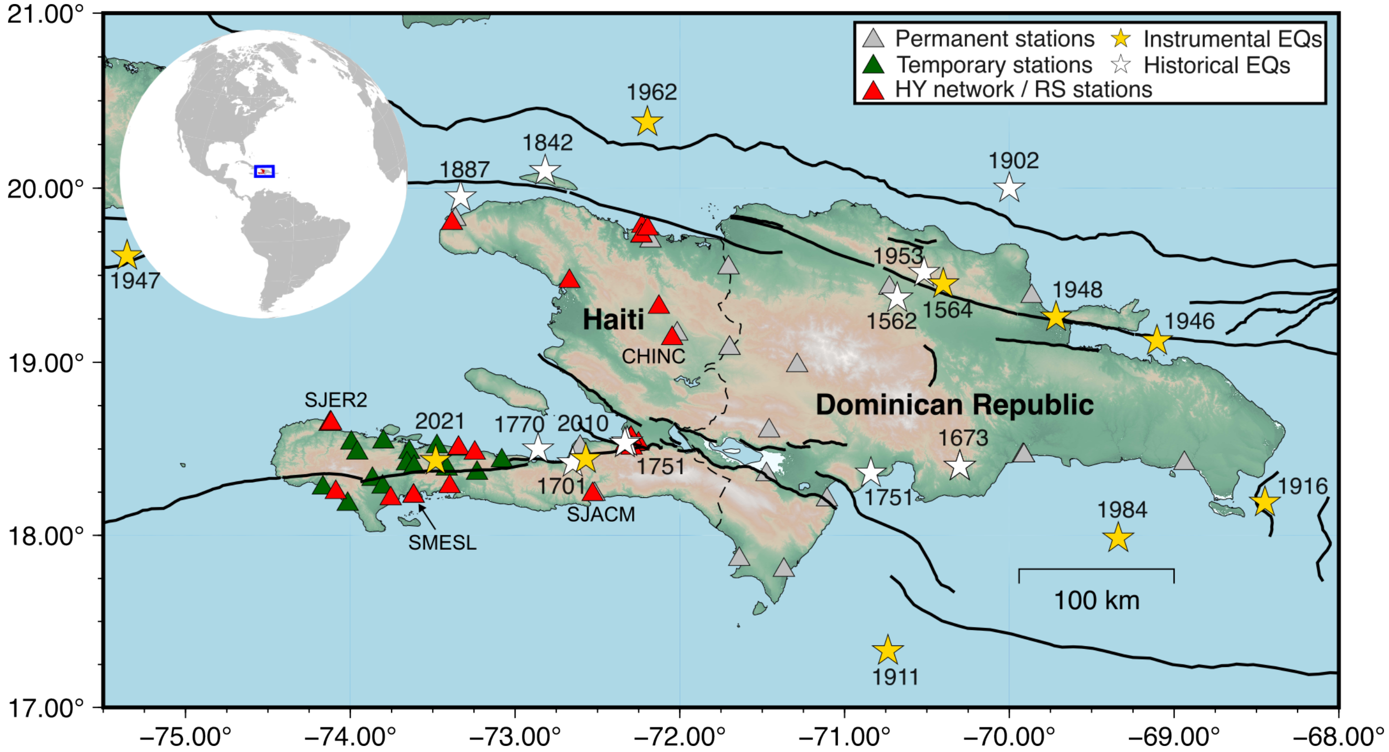

Figure 1. Map of Hispaniola showing seismic stations used in our study. Seismic stations are denoted by triangles: HY network in red, temporary deployment in green, permanent stations with publicly open data in gray. Stars mark major historical (white) and instrumentally recorded (yellow) events. Black lines indicate active fault traces Styron et al. (2020).

Alt-text: Map of Hispaniola displaying seismic stations used in our study together with major events and active fault lines in the island.

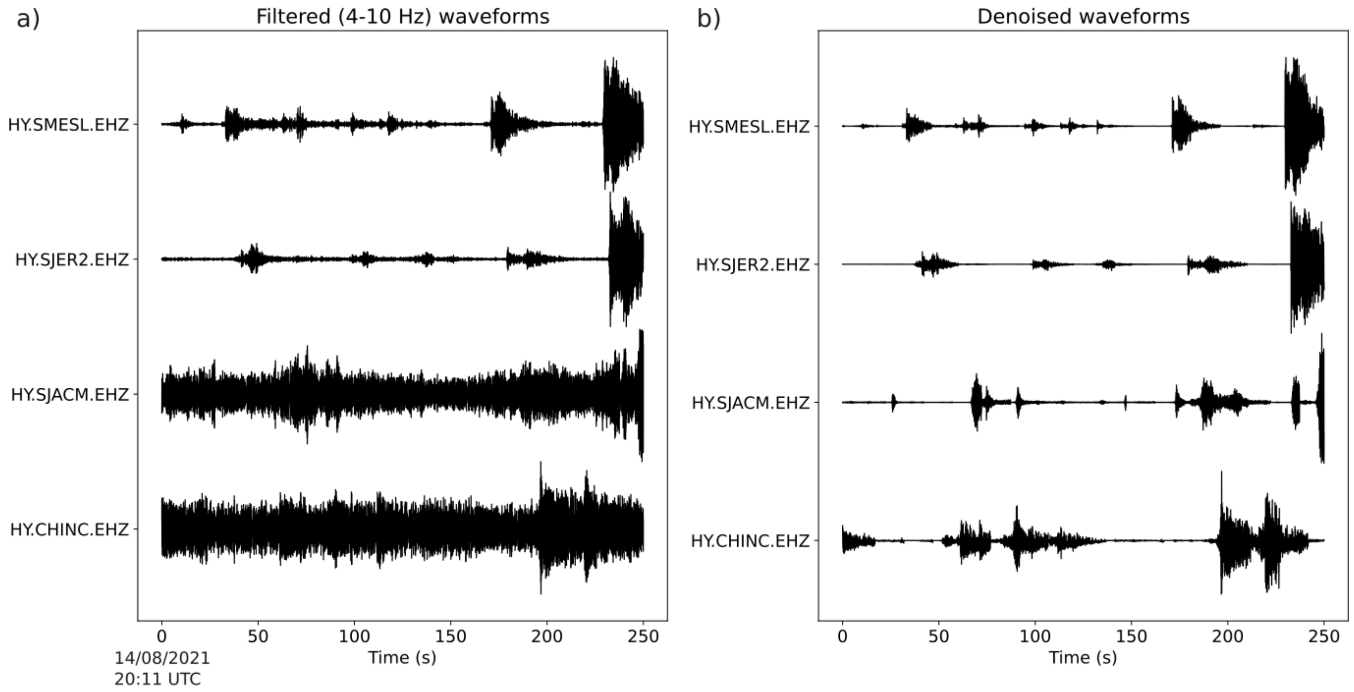

Figure 2. Examples of waveforms recorded on RS stations in Haiti. a) Bandpass filtered (4-10 Hz); b) Denoised using the original DeepDenoiser model. Station locations are shown in Figure 1.
Alt-text: Examples of denoised waveforms from RaspberryShake stations in Haiti compared to traditionally bandpass filtered waveforms.

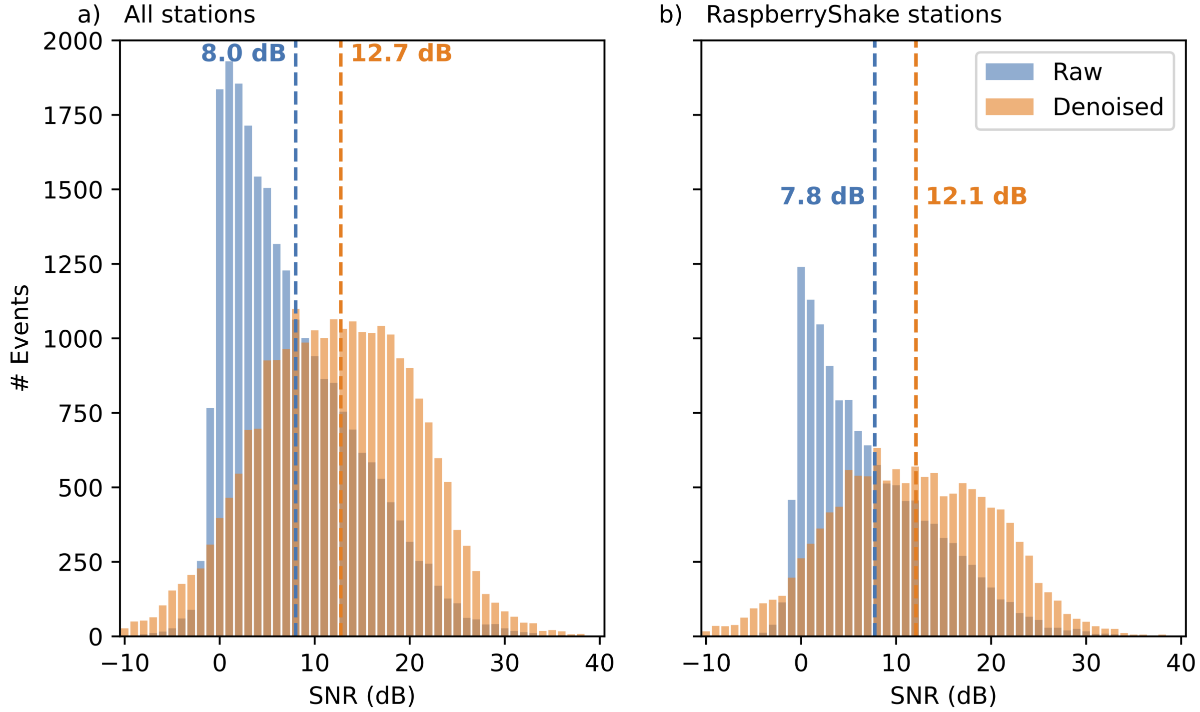

Figure 3. SNR distributions of cataloged phase picks using raw (blue) and denoised waveforms (orange). Panel (a) includes all stations on Hispaniola and panel (b) only the HY network. Negative SNRs reflect imprecise phase picks (see Figure S2). *Alt-text: SNR distributions comparing cataloged phase picks from raw (blue) and denoised (orange) waveforms. Panel a displays data from all stations, and panel b focuses on the HY network.*

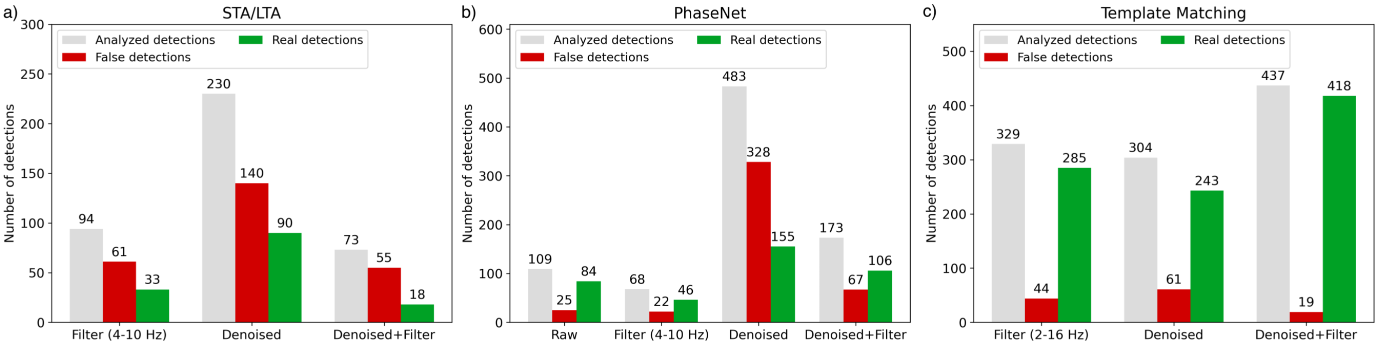

Figure 4. Comparison of detection tests using denoised and non-denoised waveforms. a) STA/LTA detection on filtered, denoised, and denoised-and-filtered waveforms. b) PhaseNet detection on raw, filtered, denoised, and denoised-and-filtered waveforms. c) Template matching detection on filtered, denoised, and denoised-and-filtered waveforms. Gray bars represent total detections, green real detections, and red bars detections.

Alt-text: Comparison of detection tests using denoised and non-denoised waveforms: panel a shows STA/LTA detections, panel b PhaseNet detections, and panel c template matching detections. Gray bars indicate total detections, green bars real detections, and red bars false detections.

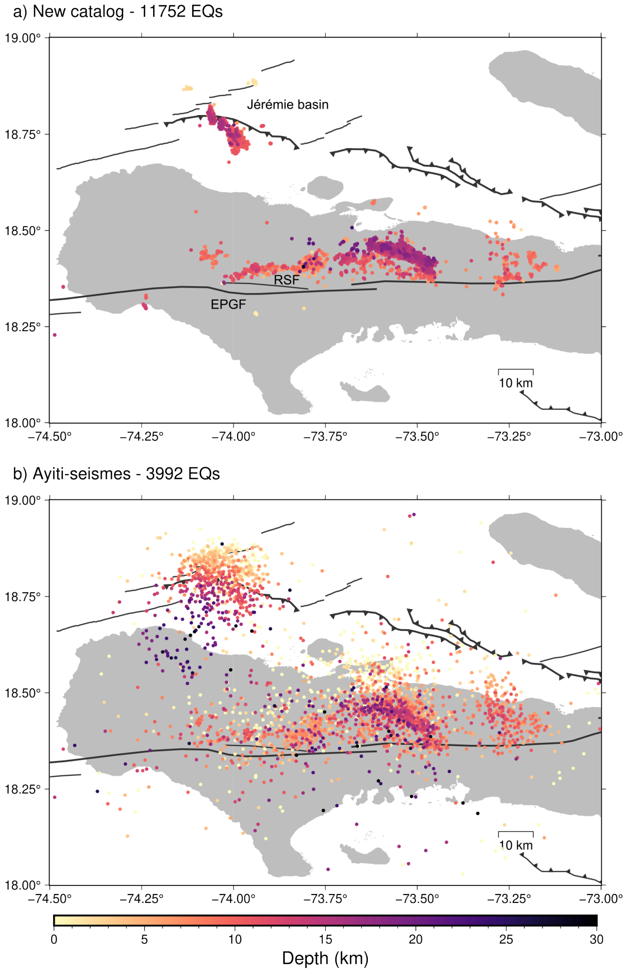

Figure 5. Catalog comparison with Ayiti-seismes earthquake catalog for 01/01/2021 to 31/12/2022. a) New catalog. b) Catalog from the Ayiti-seismes platform. Color denotes depth.
Alt-text: Comparison of our new catalog with Ayiti-seismes earthquake catalog.

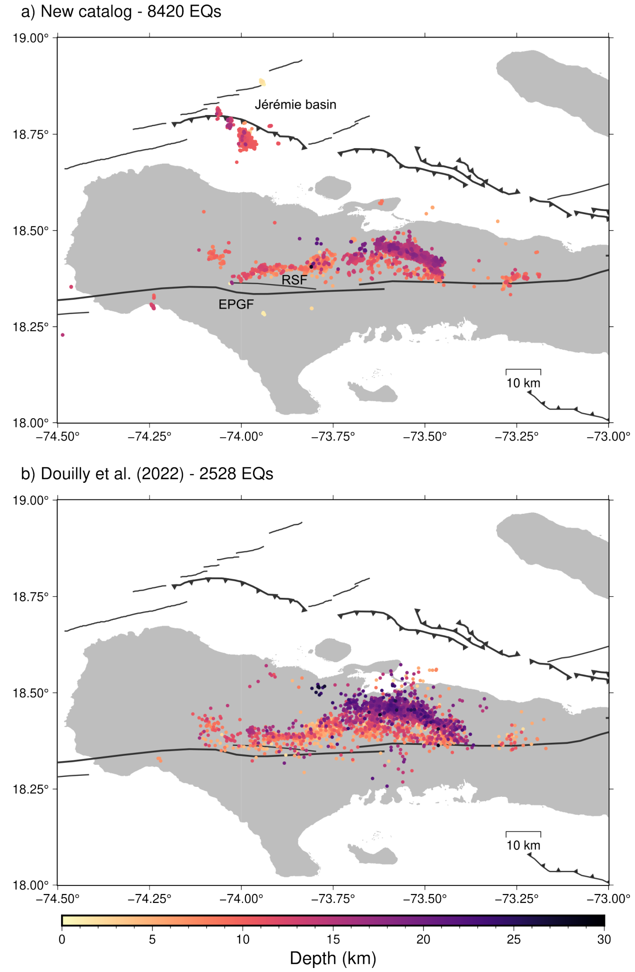

Figure 6. Catalog comparison with Douilly et al. (2022) earthquake catalog for 20/08/2021 to 30/12/2021. a) New catalog. b) Douilly et al. (2022) catalog. Color denotes depth.
Alt-text: Comparison of our new catalog with Douilly et al. (2022) earthquake catalog.

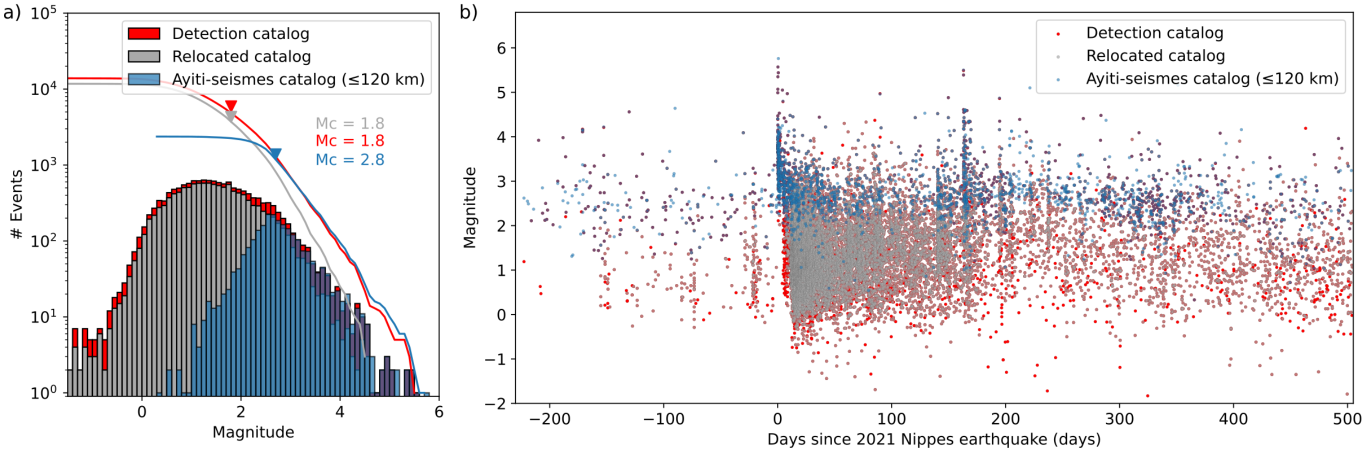

Figure 7. Magnitude distributions for the new relocated catalog (gray), detection catalog (red), and Ayiti-seismes catalog (blue). a) Magnitude-frequency distribution, with lines showing the cumulative distribution, and triangles indicate estimated magnitude of completeness using the maximum curvature method (Woessner and Wiemer, 2005). b) Magnitude distribution with time.

Alt-text: Magnitude distributions for the relocated catalog (gray), detection catalog (red), and Ayiti-seismes catalog (blue). Panel a shows the magnitude-frequency distribution with cumulative lines and completeness estimates. Panel b presents the magnitude distribution over time.

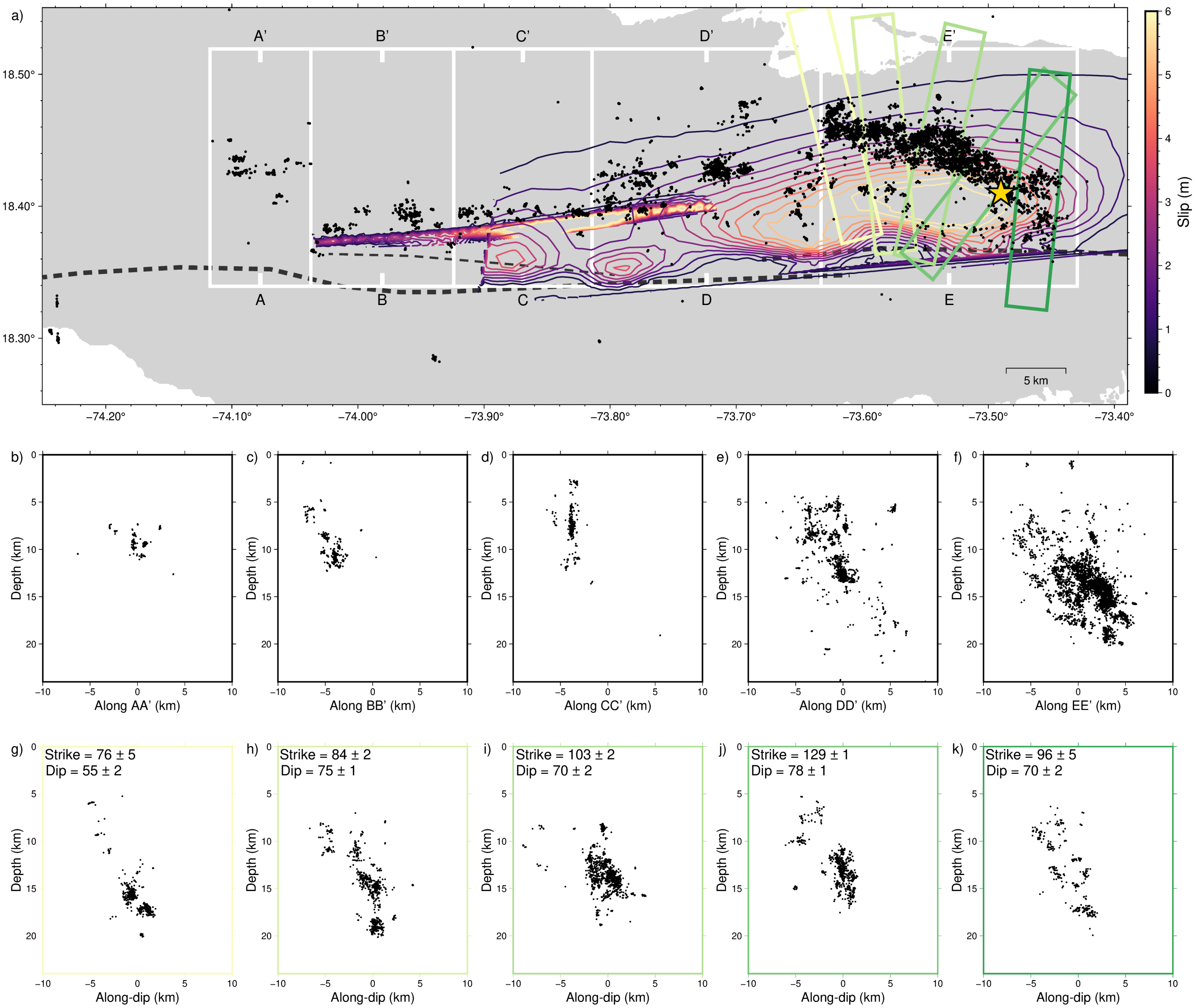

Figure 8. Spatial distribution of the seismicity in our new catalog for the 2021 $\mathrm{M_w}$ 7.2 Nippes earthquake region. a) Seismicity with co-seismic rupture slip contours from Raimbault et al. (2023) (color denotes slip amplitude in meters). Black dashed lines show faults with surface expression from Calais et al. (2023). b)-f) Cross-sections along A-A' to E-E' profiles. g)-k) Along-dip cross-sections of events within the corresponding colored rectangles in a).

Alt-text: Spatial distribution of seismicity in the 2021 Mw 7.2 Nippes earthquake region, with co-seismic rupture slip contours (panel a). Panels b-f present cross-sections along profiles A-A' to E-E', and panels g-k show along-dip cross-sections of events within the identified best planes described in the main text.

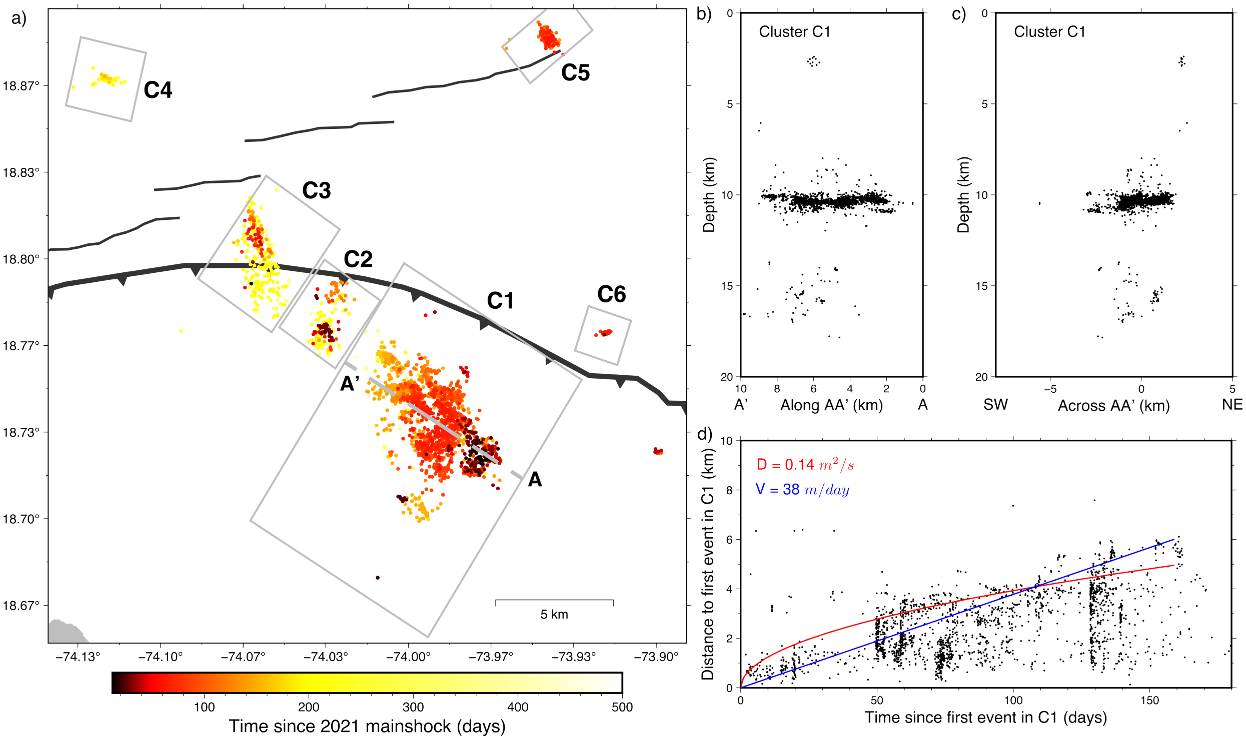

Figure 9. Jérémie basin clusters. a) Events in the new catalog colored by occurrence time and faults from Calais et al. (2023). b) Cross-section of cluster C1 along A-A'. c) Cross-section across A-A'. d) Distance of events to the first event in C1 versus time. Blue and red lines show the best fit using linear migration and fluid diffusion models, respectively.

Alt-text: Seismic clusters in the Jérémie basin, illustrating occurrence time and faults (panel a). Panels b and c present cross-sections of cluster C1. Panel d shows event distribution in C1 over time, with best fit models for linear migration and fluid diffusion.

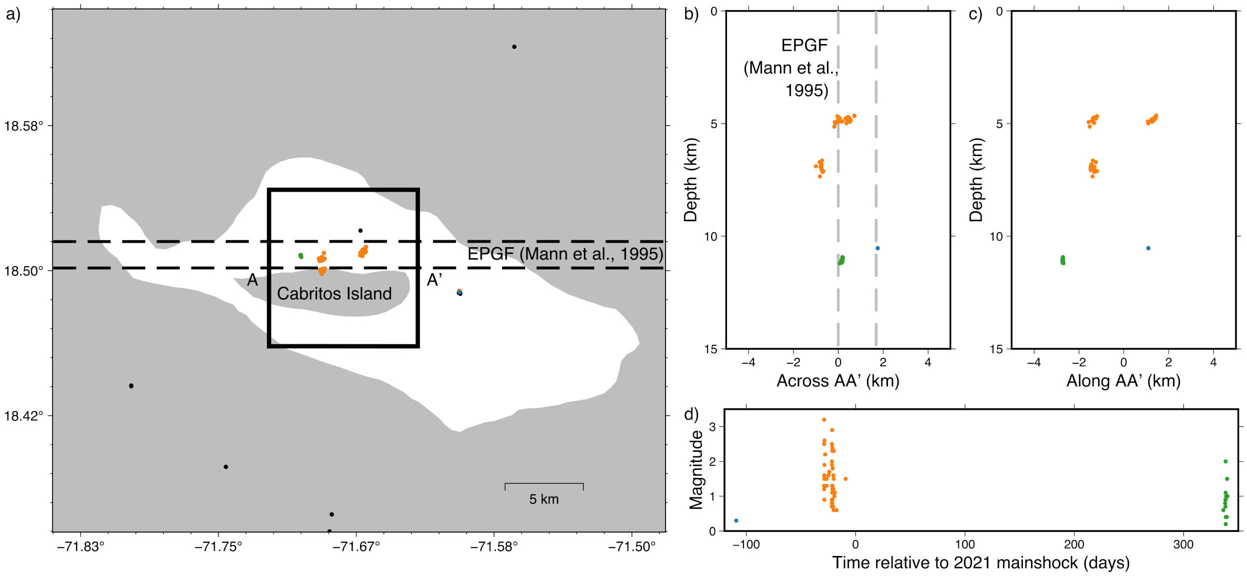

Figure 10. Seismicity in the Lake Enriquillo area. a) Events in the new catalog, colored by temporal groups; dashed black lines trace the EPGF continuation proposed by Mann et al. (1995). b) North–south cross-section of the seismicity with the proposed EPGF continuation shown in gray. c) West-east cross-section. d) Magnitude distribution with time.

Alt-text: Seismicity in the Lake Enriquillo area (panel a). Panel b presents a north-south cross-section of seismic events, with the proposed EPGF continuation by Mann (1995) highlighted in gray. Panel c features a west-east cross-section, and panel d illustrates the magnitude distribution over time.

Supplemental material to "Enhancing earthquake monitoring with deep learning in Haiti"

Miguel Neves*[1], Quentin Bletery[1], Françoise Courboulex[1], David Ambrois[1], Jérôme Chèze[1], Tony Monfret[1,2], Steeve Symithe[3], Sylvert Paul[1,3], Louis De Barros[1], Bryan Raimbault[4], and Éric Calais[5]

Used seismic stations and source-station distances considered

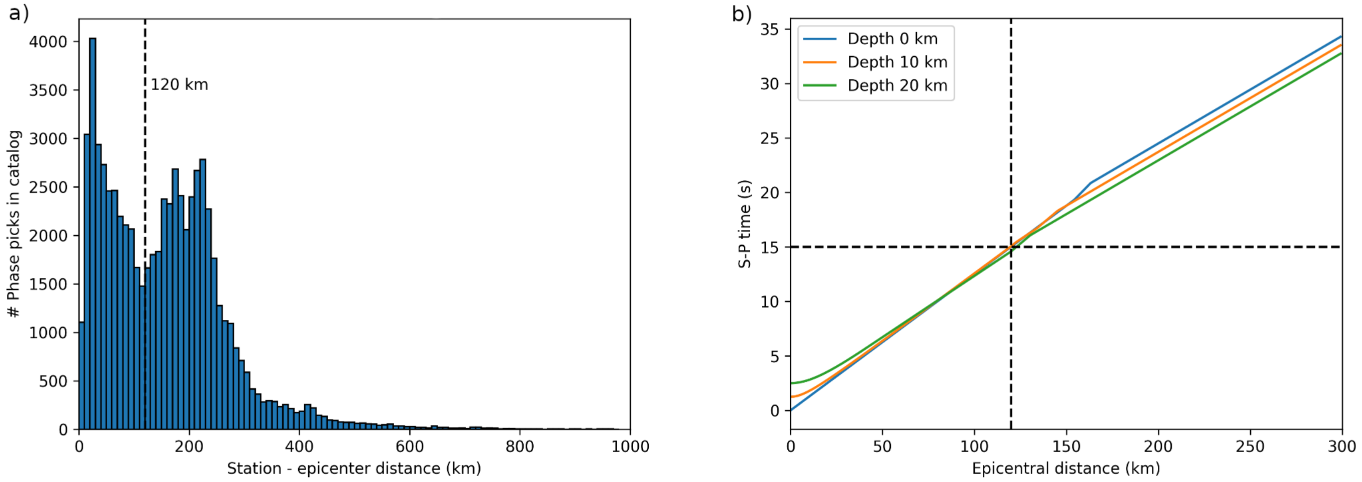

Figure S1. Phase picks used in our study and selection of a 16 s template matching window. a) Distribution of phase picks in the Ayiti-seismes catalog as a function of epicentral distance to the recording station. Dashed black line marks 120 km distance, the maximum epicentral distance considered in our study. b) Modeled S-P times as a function of epicentral distance for different depths considering the IASPEI91 velocity model (Kennett and Engdahl, 1991). Based on the model we choose to use a 16 s window for our template matching procedure.

---

1. Observatoire de la Côte d'Azur, Université Côte d'Azur, IRD, CNRS, Geoazur, France, https:// orcid.org/0000-0002-8581-8551 (MN) https://orcid.org/0000-0002-9796-5487 (QB) https:// orcid.org/0000-0002-4467-9102 (FC) https:// orcid.org/0000-0003-1155-5645 (DA) https:// orcid.org/0000-0002-7644-3989 (JC) https:// orcid.org/0000-0002-4521-0357 (TM) https:// orcid.org/0000-0003-4132-7635 (SP) https:// orcid.org/0000-0002-5541-9162 (LDB); 2. Barcelona Center for Subsurface Imaging, Institut de Ciències del Mar (ICM), CSIC, Barcelona, Spain, https://orcid.org/0000-0002-4521-0357 (TM); 3. URGéo, Faculté des Sciences, Université d'État d'Haïti, Port-au-Prince, Haïti, https://orcid.org/0000-0003-1133-202X (SS) https://orcid.org/0000-0003-4132-7635 (SP); 4. Jet Propulsion Laboratory, California Institute of Technology, Pasadena, CA, USA, https://orcid.org/0000-0001-9561-6171 (BR); 5. Département de Géosciences, École normale supérieure, Université PSL, Paris, France, https://orcid.org/0000-0002-5935-8117 (EC)

*Corresponding author: migueljgneves@gmail.com

TABLE S1.

Seismic stations used in this study with first and last available dates during the study interval.

Network	Station	Channel code	First available date	Last available date	Number of available days
AY	PAPH1	HH	06.05.2022	31.12.2022	238
CN	LGNH	HH	01.01.2021	31.12.2022	652
CU	SDDR	BH	14.08.2021	31.12.2022	385
DR	SC01	BH	14.08.2021	31.12.2022	428
DR	SDD	BH	14.08.2021	31.12.2022	400
HY	CDELM	EH	09.02.2021	09.02.2021	1
HY	CGONA	EH	14.01.2021	31.12.2022	590
HY	CHINC	EH	23.07.2021	23.12.2022	173
HY	CMOCA	EH	10.10.2022	31.12.2022	81
HY	CPACO	EH	01.01.2021	31.12.2022	672
HY	CTORC	EH	10.02.2021	20.10.2021	98
HY	NCAP1	EH	24.07.2021	22.08.2022	376
HY	NCORM	EH	01.01.2021	31.12.2022	350
HY	NMSNI	EH	14.04.2021	07.10.2021	106
HY	NPIGN	EH	01.01.2021	08.12.2022	460
HY	NQBME	EH	16.04.2021	26.12.2022	258
HY	PPIM	EH	12.06.2022	30.12.2022	136
HY	SANSE	EH	25.03.2021	17.08.2021	57
HY	SAQUI	EH	19.08.2021	01.12.2022	398
HY	SCAYE	EH	01.01.2021	29.12.2022	152
HY	SJACM	EH	11.03.2021	20.08.2022	244
HY	SJER1	EH	09.02.2022	21.11.2022	254
HY	SJER2	EH	01.01.2021	31.12.2022	407
HY	SJER3	EH	16.06.2022	07.10.2022	7
HY	SMESL	EH	01.01.2021	31.12.2022	610
HY	SPRIV	EH	18.08.2021	04.07.2022	174
LO	LOBH	EH	14.08.2021	31.12.2022	410
LO	LODA2	EH	14.08.2021	31.12.2022	498
LO	LODU1	EH	14.08.2021	31.12.2022	505
LO	LONA2	EH	14.08.2021	31.12.2022	406
LO	LONE3	EH	14.08.2021	31.12.2022	497
LO	LOVI	EH	14.08.2021	31.12.2022	498
Z2	BFIN	HH	25.08.2021	31.12.2022	494
Z2	CAMPP	HH	02.10.2021	31.12.2022	400
Z2	CAVA	HH	26.08.2021	31.12.2022	379
Z2	CHARD	HH	27.08.2021	31.12.2022	492
Z2	HASL	HH	22.08.2021	31.12.2022	375
Z2	HBAR	HH	18.08.2021	01.02.2022	142
Z2	LBOR	HH	27.08.2021	02.09.2022	26
Z2	PBEAU	HH	26.08.2021	31.12.2022	493
Z2	PEST	HH	25.08.2021	31.12.2022	363
Z2	ROCH	HH	26.08.2021	31.12.2022	493
Z2	SALO	HH	02.10.2021	31.12.2022	380
Z2	STTHE	HH	26.08.2021	31.12.2022	491
Z2	TROU	HH	25.08.2021	31.12.2022	494
Z2	UR01	HH	21.01.2022	21.02.2022	32
Z2	UR02	HH	21.01.2022	22.02.2022	33
Z2	UR03	HH	21.01.2022	21.02.2022	30
Z2	UR04	HH	25.01.2022	21.02.2022	28

Signal-to-noise ratio analysis of cataloged phase picks

As part of our assessment of the impacts of the DeepDenoiser model in our dataset, we apply the denoiser to every P-phase pick listed in the Ayiti-seismes catalog. We calculate the signal-to-noise ratio (SNR) of both the raw and denoised signals and compare results in Figure 3. We calculate SNR using a 5 s window after the phase pick as signal, and a 5 s window prior as noise. Our results show an average SNR improvement of 4.7 dB in the denoised signals. However our estimates also reveal a group of signals with negative SNR when using the raw signals, which become even more negative after denoising. A visual inspection of these events (Figure S2) reveals that they correspond to imprecisely picked phase arrivals in the catalog. These incorrect picks exhibit a systematic delay to the actual P-phase arrival, likely due to the STA/LTA system, which becomes more evident after denoising.

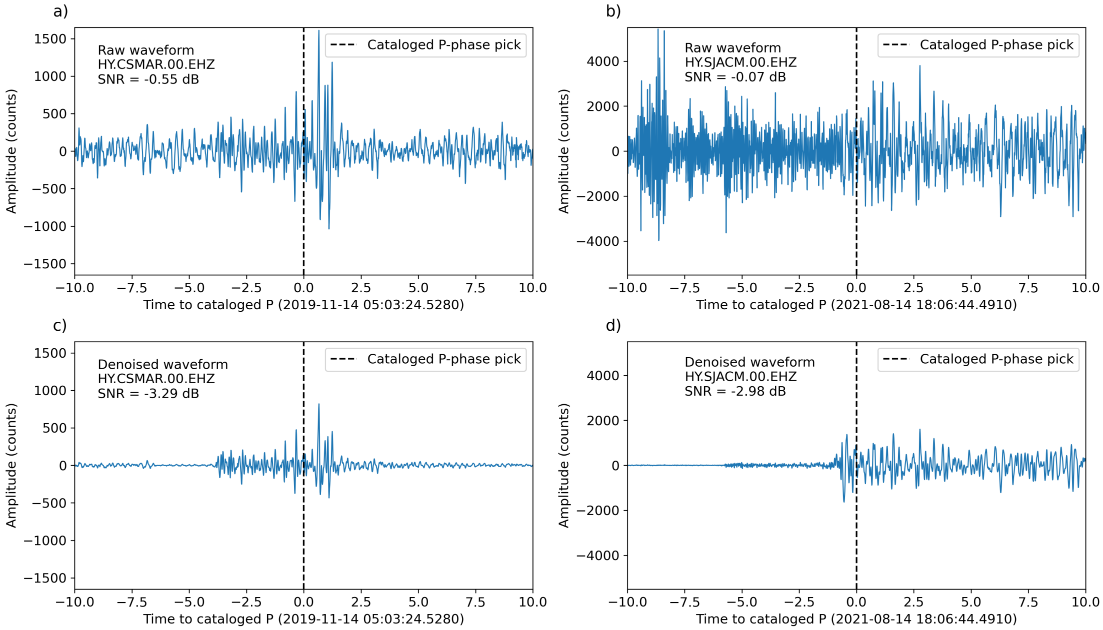

Figure S2. Example of catalog P-phase picks showing a negative estimated SNR. (a) and (b) show the raw waveforms (only with trend removed) for two different events at stations CSMAR and SJACM, respectively, and (c) and (d) the corresponding denoised waveform. The P-phase pick listed in the Ayiti-seismes catalog is marked at 0 s.

Magnitude Estimation

As noted in previous studies (Zhu et al., 2019; Yang et al., 2022), DeepDenoiser tends to distort waveforms and clip peak amplitudes. Thus, the estimated magnitudes are not comparable to those estimated from the original waveforms. Therefore, we follow a different approach and apply relative magnitude estimation, a method commonly used in template matching detection studies (e.g. Peng and Zhao, 2009; Neves et al., 2022, 2024).

Relative magnitudes can be estimated by comparing the waveforms of a new detection with those of a cataloged event using:

$$M_{New} = M_{Cat.Event} + c \times \log_{10} \alpha, \tag{S1}$$

where M_{New} is the estimated magnitude, $M_{Cat.Event}$ is the magnitude of the cataloged earthquake, c is a calibration constant, and α is the amplitude ratio between the new detection and the cataloged event. We calculate the amplitude ratio by comparing the peak amplitudes of the new detection and the cataloged event following the method described in Neves et al. (2022) based on Shelly et al. (2016)'s method, but with amplitude ratios determined by the peak amplitude instead of using a principal component fit of the waveforms. c is determined by comparing each cataloged event's estimated magnitude and peak amplitude with those of all other cataloged events that correlate with a cross-correlation coefficient ≥ 0.6, and then fitting the resulting pairs by least-squares. We determine c for bandpass-filtered, denoised, and bandpass-filtered-plus-denoised waveforms, finding a consistent value of 0.89 for all cases (Figure S3).

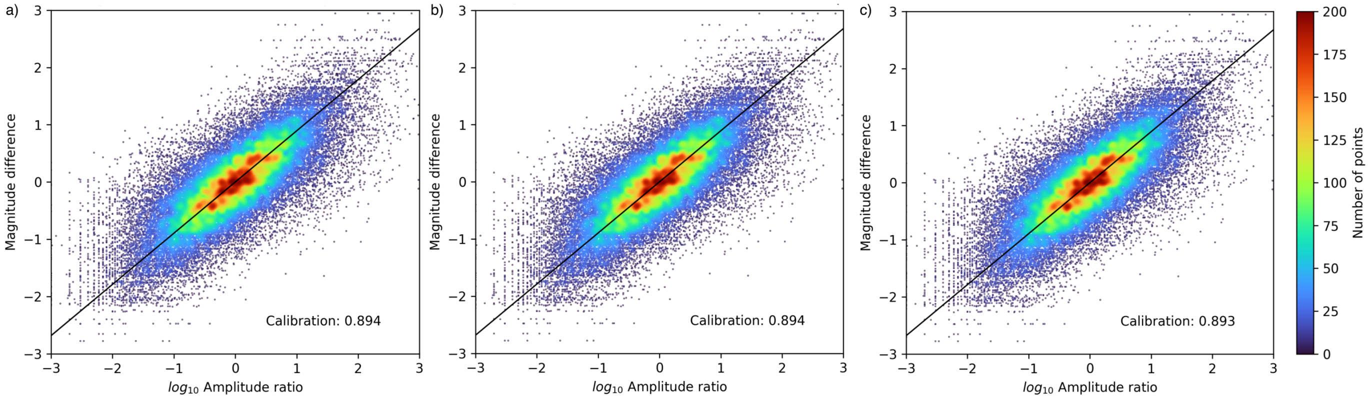

Figure S3. Magnitude calibration for relative magnitude measurements. Figures show the distribution of similar templates magnitude differences as a function of the corresponding templates logarithm of peak amplitude ratio for a) raw waveforms, b) band-pass filtered 2-16 Hz waveforms and c) denoised waveforms. Similar calibration factors are estimated for the three cases, suggesting that DeepDenoiser distorts the waveforms in similar ways, retaining the relative amplitude information.

33 ## Relocated catalog and missed earthquake detections

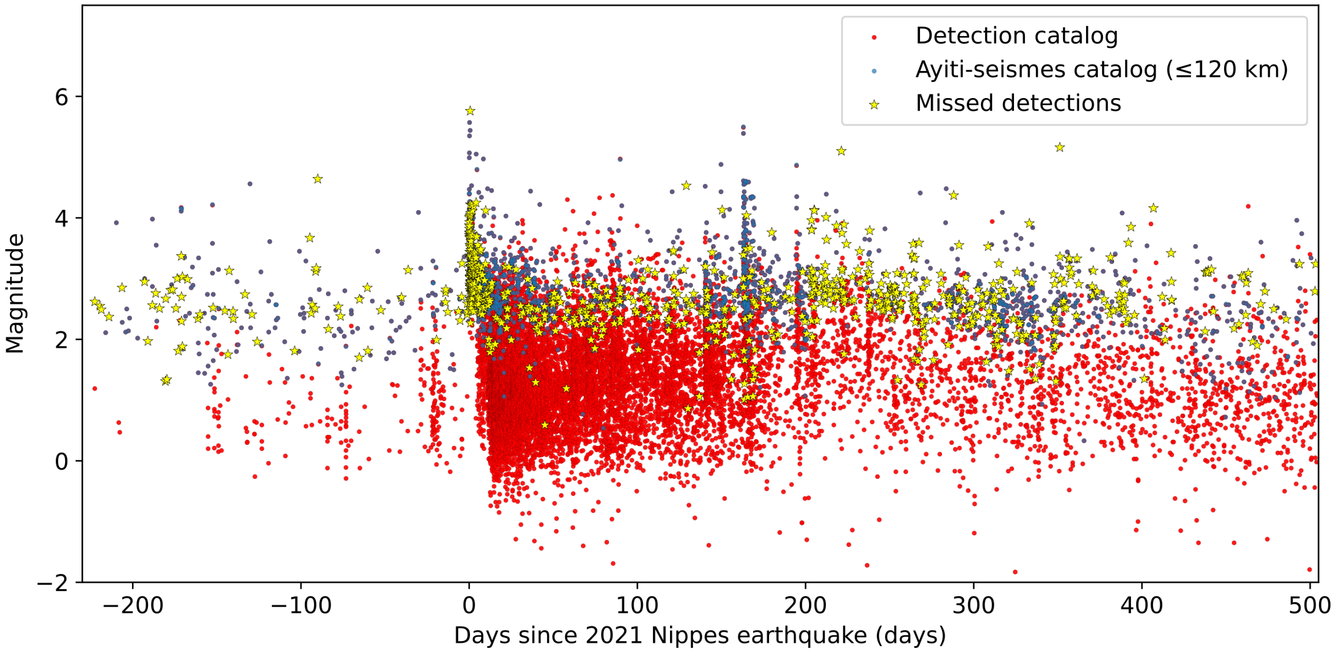

Figure S4. Detections missed by our denoising plus template matching workflow. Magnitude distribution with time of the detection catalog (red) and the Ayiti-seismes catalog (blue). Missed detections due to the requirement of at least 4 recording stations in a 120 km radius are marked by yellow stars.

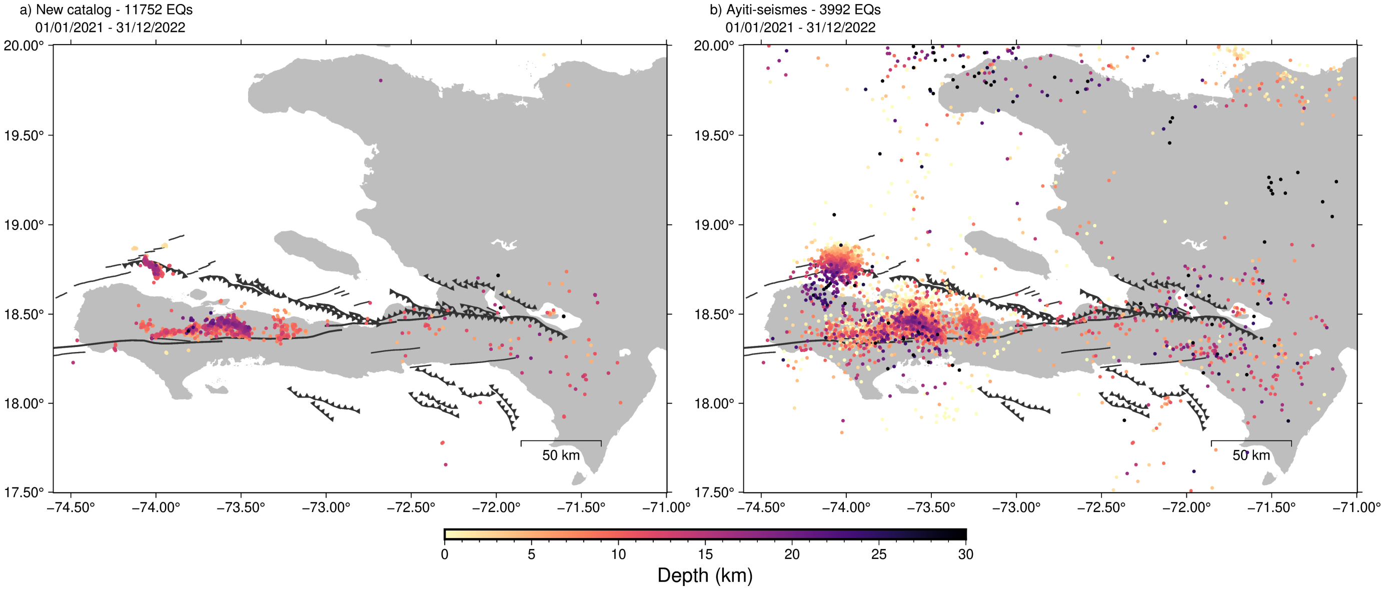

Figure S5. Catalog comparison of the entire area covered by our new relocated catalog with the Ayiti-seismes earthquake catalog. a) New catalog resulting from denoising, template matching detection, and cross-correlation relocation. b) Catalog from the Ayiti-seismes platform. Color denotes event depth.

Additional Jérémie basin clusters

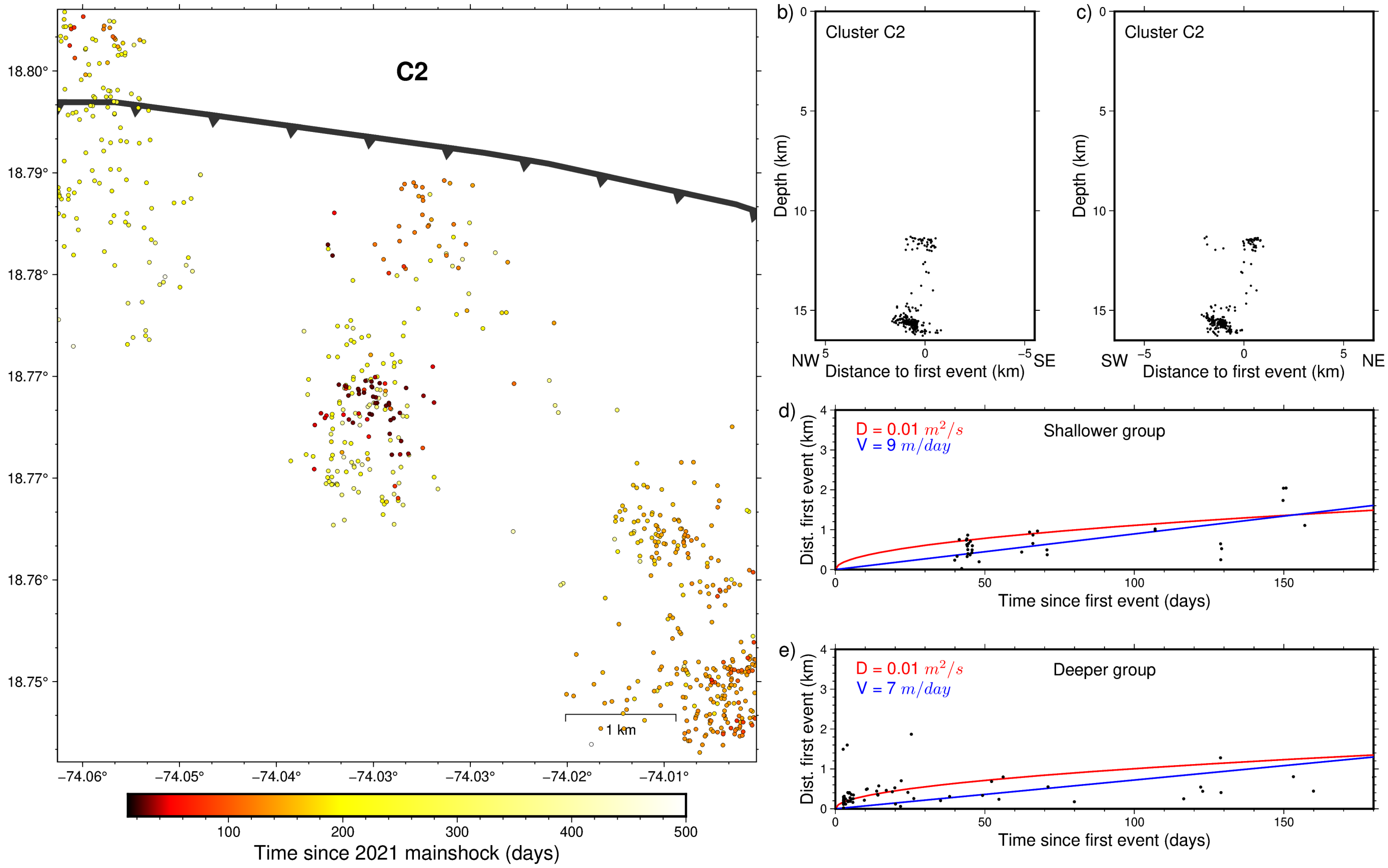

Figure S6. Jérémie basin C2 cluster (see Figure 9). a) Hypocenter distances to the first event in the cluster as a function of time and faults with surface expression identified in Calais et al. (2023). b) Cross-section of major cluster in the area along NW-SE direction. c) Cross-section along SW-NE direction. d) Distribution of the shallower events (above 14 km) in the cluster with time in relation to the first event. Red line denotes the best fit to a square root front and blue line the best fit to a linear front. e) Same as (d) for the deeper events (below 14 km depth).

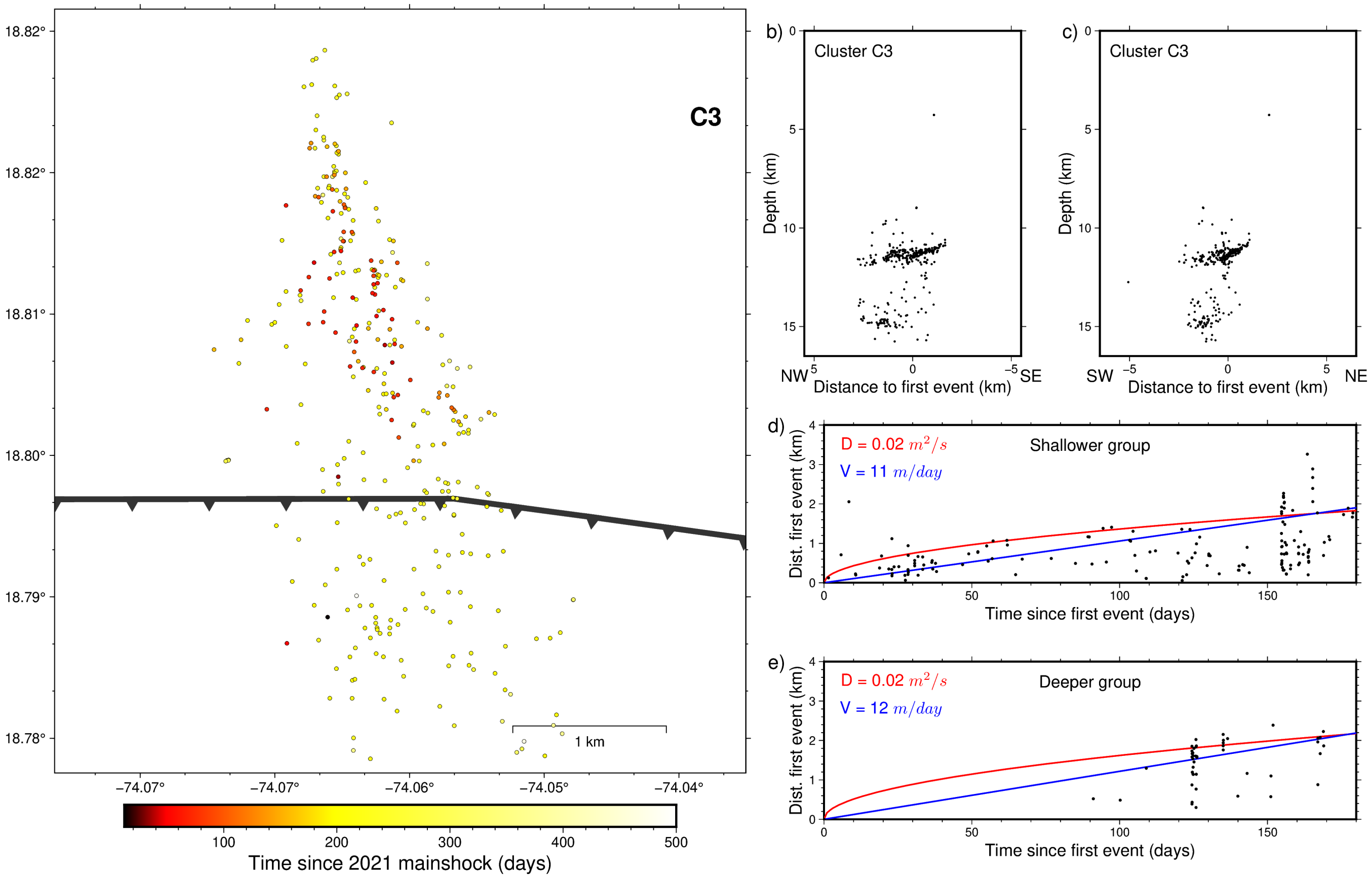

Figure S7. Jérémie basin C3 cluster (see Figure 9). a) Hypocenter distances to the first event in the cluster as a function of time and faults with surface expression identified in Calais et al. (2023). b) Cross-section of major cluster in the area along NW-SE direction. c) Cross-section along SW-NE direction. d) Distribution of the shallower events (above 14 km) in the cluster with time in relation to the first event. Red line denotes the best fit to a square root front and blue line the best fit to a linear front. e) Same as (d) for the deeper events (below 14 km depth).

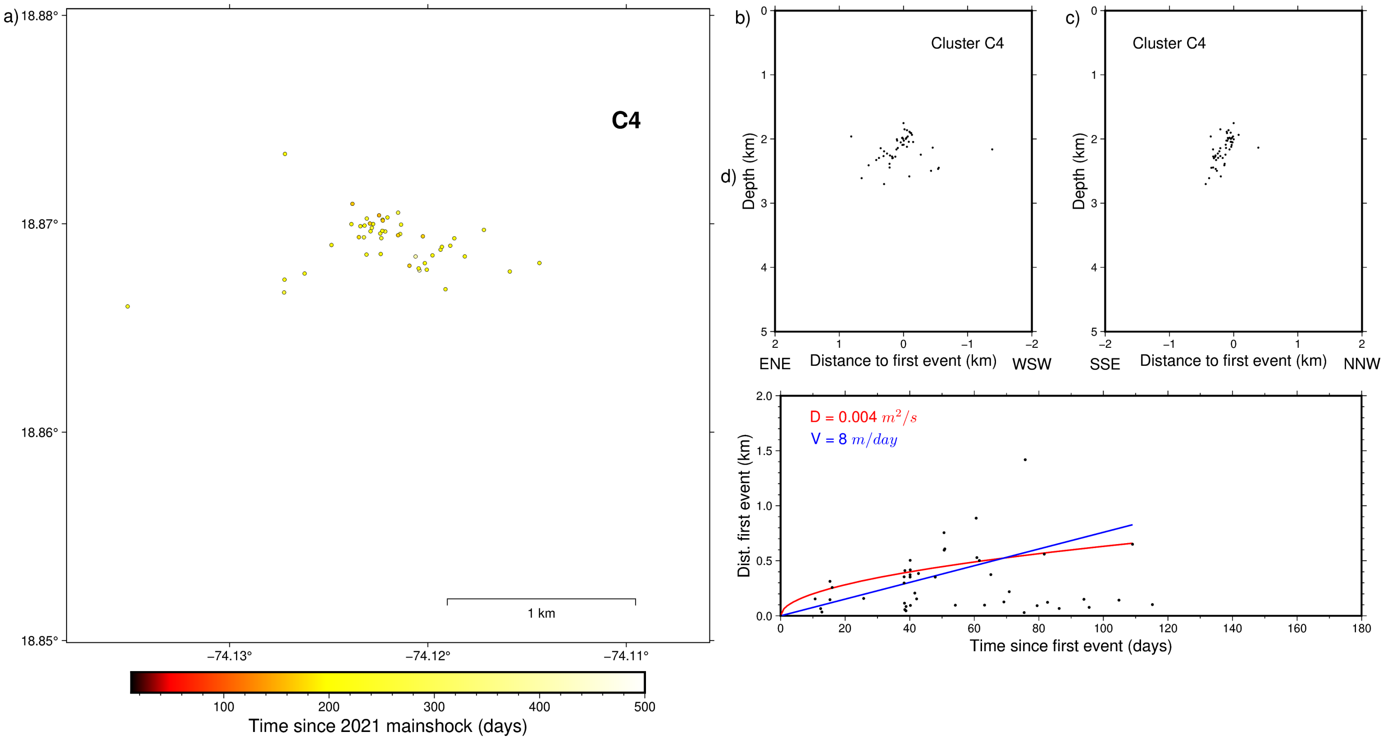

Figure S8. Jérémie basin C4 cluster (see Figure 9). a) Hypocenter distances to the first event in the cluster as a function of time. b) Cross-section of major cluster in the area along ENE-WSW direction. c) Cross-section along SSE-NNW direction. d) Distribution of events in the cluster with time in relation to the first event. Red line denotes the best fit to a square root front and blue line the best fit to a linear front.

Description of supplemental datasets

Supplemental Dataset S1: publication_detection_catalog.txt

Catalog containing detected events using the template matching detection on denoised waveforms followed by a bandpass filter. It includes events only associated with local templates.

File format: DetID, YYYY, MM, dd, hh, mm, ss.sss, lat, lon, depth, mag

DetID: detection numeric identifier

YYYY: year of earthquake origin time

MM: month

dd: day

hh: hour

mm: minute

ss.sss: seconds

lat: latitude(degrees)

lon: longitude(degrees)

depth: depth in km

mag: earthquake magnitude

Supplemental Dataset S2: publication_relocation_catalog.txt

Catalog containing relocated events using cross-correlation-derived differential travel-time information.

File format: DetID, YYYY, MM, dd, hh, mm, ss.sss, lat, lon, depth, e_xx, e_yy, e_z, rms,mag

DetID: detection numeric identifier

YYYY: year of earthquake origin time

MM: month

dd: day

hh: hour

mm: minute

ss.sss: seconds

lat: latitude(degrees)

lon: longitude(degrees)

depth: depth in km

ex: North-South uncertainty (m)

ey: East-West uncertainty (m)

ez: depth uncertainty (m)

rms: root mean square of the differential times

mag: earthquake magnitude

References

Calais, E., S. J. Symithe, and B. M. de Lépinay (2023). Strain partitioning within the caribbean–north america transform plate boundary in southern haiti, tectonic and hazard implications. *Bulletin of the Seismological Society of America* **113**(1), 131–142.

Kennett, B. L. N. and E. R. Engdahl (1991). Traveltimes for global earthquake location and phase identification. *Geophysical Journal International* **105**(2), 429–465.

Neves, M., L. Y. Chuang, W. Li, Z. Peng, P. M. Figueiredo, and S. Ni (2024). Complex rupture dynamics of the extremely shallow august 2020 m5. 1 sparta, north carolina earthquake. *Communications Earth & Environment* **5**(1), 163.

Neves, M., Z. Peng, and G. Lin (2022, 11). A high-resolution earthquake catalog for the 2004 mw 6 parkfield earthquake sequence using a matched filter technique. *Seismological Research Letters* **94**(1), 507–521.

Peng, Z. and P. Zhao (2009). Migration of early aftershocks following the 2004 Parkfield earthquake. *Nature Geoscience* **2**(12), 877–881.

Shelly, D. R., W. L. Ellsworth, and D. P. Hill (2016). Fluid-faulting evolution in high definition: Connecting fault structure and frequency-magnitude variations during the 2014 Long Valley Caldera, California, earthquake swarm. **121**(3), 1776–1795.

Yang, L., X. Liu, W. Zhu, L. Zhao, and G. C. Beroza (2022). Toward improved urban earthquake monitoring through deep-learning-based noise suppression. *Science Advances* **8**(15), eabl3564.

Zhu, W., S. M. Mousavi, and G. C. Beroza (2019). Seismic Signal Denoising and Decomposition Using Deep Neural Networks. *IEEE Transactions on Geoscience and Remote Sensing* **57**(11), 9476–9488.